A generalized finite volume method for density driven flows in porous media

Yueyuan Gao, Danielle Hilhorst, Huy Cuong Vu Do

A generalized finite volume method for density driven flows in porous media

Yueyuan Gao [*], Danielle Hilhorst[†], and Huy Cuong Vu Do [‡*]

December 24, 2020

Abstract. We apply a semi-implicit scheme in time together with a generalized finite volume method for the numerical solution of density driven flows in porous media; it comes to solve a nonlinear convection-diffusion parabolic equation for solute transport together with an elliptic equation for the pressure. In the first part, we compute the solutions for three specific problems: a problem involving a rotating interface between salt and fresh water, Henry's problem and a three dimensional saltpool problem. In the second part, we take the heat transfer into account and perform simulations for a system from the documentation of SEATWAT. We use adaptive meshes, based upon square volume elements in space dimension two and cubic volume elements in space dimension three.

Keywords: Density driven flows in porous media; The generalized finite volume method SUSHI; Adaptive meshes; Heat transfer.

1 Introduction

In this paper, we present results which have been obtained in the context of an exploratory project of CNRS (PEPS ECODEVA) on the numerical simulation of flows with variable density for the production of lithium batteries. More precisely, the purpose of this project is related to the exploitation of lithium deposits in salt lakes, also known as "Salars". In recent years, lithium has become a strategic element for industrial countries because it is the basic element of lithium-ion batteries used for hybrid and electric vehicles. Therefore its production has become of high interest for all major groups involved in the car industry as well as suppliers of these groups. Currently the largest deposit in the world is the Salar Uyuni, in the department of Potosí in South-West Bolivia. This deposit represents one third of the world

[*]MathAM-OIL, Advanced Industrial Science and Technology Tohoku c/o AIMR, Tohoku University, 2-1-1 Katahira, Aoba-ku, Sendai 980-8577, Japan

[†]CNRS, Laboratoire de Mathématique, Analyse Numérique et EDP, Université Paris-Saclay, F-91405 Orsay Cedex, France

[‡]Faculty of Mathematics and Computer Science. University of Science, VNU-HCMC. Ho Chi Minh City, Vietnam

resources. In March 2008, Bolivia has authorized the exploitation, however reserving this right ot its nationals. Chile has the second largest deposit with the Salar Atacama and it has become the world's largest exporter since 1997, with the German company Chemettal as main operator. Argentina also has a lithium deposit, the Salar Hombre Muerto, which is located in the northwest of the country. Other Salar areas of the Altiplano of Argentina provide mining exploitation concessions to foreign companies, among whom European groups.

Other deposits are exploited, including salt lakes in Tibet as well as mines in Australia, Russia and the United States. They are not accessible to European operators. The largest deposits are either clusters of crystallized salt (solid) or lenses of supersaturated salt water created by evaporation under endorheic conditions (which are not led to a superficial network reaching the sea). The latter type of deposit is that of salars of the Andean Altiplano. Rational exploitation implies mastering these special aqueous flows whose density depends on the concentration of salts (lithium included). An operating technique consists in sweeping the reservoir with fresh water in order to obtain a maximal recovery without earthworks and with a minimal impact on fluid levels, and thus a minimal impact on the environment. This explains the need of implementing research methodologies and techniques from hydrogeology. The purpose here is to extract salt water which contains lithium. In a later stage, the lithium will be separated from the salt water.

From a mathematical viewpoint, it amounts to studying a coupled system describing the interaction between flow and transport in a porous medium. More specifically, the equations governing density-dependent transport are the Darcy's law (1.1a), the continuity equation for the fluid (1.1b), the continuity equation for the solute (1.1c), which are given as

$$\begin{cases} \mathbf{q} = -\dfrac{k}{\mu}\big(\nabla p - \rho(c)\mathbf{g}\big) & \text{in } \Omega \times (0,T), \qquad (1.1a) \\ \theta \dfrac{\partial \rho(c)}{\partial t} + \nabla \cdot \big(\mathbf{q}\rho(c)\big) = \rho_s Q_s & \text{in } \Omega \times (0,T), \qquad (1.1b) \\ \theta \dfrac{\partial \big(\rho(c)c\big)}{\partial t} + \nabla \cdot \big(\mathbf{q}\rho(c)c - \rho(c)D\nabla c\big) = \omega_s \rho_s Q_s & \text{in } \Omega \times (0,T), \qquad (1.1c) \end{cases}$$

together with suitable boundary conditions of the form

$$\begin{cases} c = c_D(\mathbf{x},t) & \text{on } \partial\Omega_D^c \times (0,T), \\ \dfrac{\partial c}{\partial n} = \bar{c}_N(\mathbf{x},t) & \text{on } \partial\Omega_N^c \times (0,T), \\ p = p_D(\mathbf{x},t) & \text{on } \partial\Omega_D^p \times (0,T), \\ \mathbf{q}\cdot\mathbf{n} = \bar{q}_N(\mathbf{x},t) & \text{on } \partial\Omega_N^p \times (0,T), \end{cases} \qquad (1.2)$$

with $\partial\Omega = \overline{\partial\Omega_D^c} \bigcup \overline{\partial\Omega_N^c} = \overline{\partial\Omega_D^p} \bigcup \overline{\partial\Omega_N^p}$ where $\partial\Omega_D^c$ and $\partial\Omega_D^p$ correspond to Dirichlet boundary conditions and $\partial\Omega_N^c$ and $\partial\Omega_N^p$ correspond to Neumann boundary condition for the concentration and the pressure respectively. The initial condition is given by $c(\mathbf{x},0) = c_0(\mathbf{x})$ in Ω. $\mathbf{q}$ represents the velocity of the flow, p the pressure, and c the concentration of a transported species. The porosity θ is the fraction of the voids (empty spaces) over the total volume, D the dispersion-diffusion tensor, k the permeability, μ the dynamic viscosity, ρ the density, and $\mathbf{g}$ is the gravity. Q_s model the source or sink term of the fluid with density ρ_s. ω_s is

the solute mass fraction. We also apply the constitutive equation relating fluid density to concentration for dilute solutions under isothermal conditions, which can be expressed as

$$\rho(c) = \rho_0(1 + \bar{a}c) \tag{1.3}$$

where $\bar{a} = \rho_{\max}/\rho_0 - 1$ [6].

We refer to [1] and [3] for modeling aspects. As far as the numerical methods are concerned, Hilhorst et al. [7] have discussed the numerical approximation of system (1.1) by means of the standard finite volume method. However, discretizing the diffusion terms with this method is only applicable with conforming meshes satisfying an orthogonality condition. The generalized finite volume method SUSHI permits to perform computations on rather general nonconforming meshes (cf. Definition 2.1 below), for instance in the case of configurations which occur when using adaptive meshes involving squares or cubes of different sizes. These adaptive meshes permit precise numerical computations with a smaller number of volume elements. We refer to the Section 2.2 for a more detailed discussion.

In order to apply the generalized finite volume method SUSHI, we set $w := w(c) = \int_0^c \rho(s)ds$, $m(w) = \rho(c)c$ and $\varrho(w) = \rho(c)$ and rewrite the system in the form

$$\begin{cases} \mathbf{q} = -\dfrac{k}{\mu}\big(\nabla p - \varrho(w)\mathbf{g}\big) & \text{in } \Omega \times (0,T) \\ \theta\dfrac{\partial \varrho(w)}{\partial t} + \nabla \cdot \big(\mathbf{q}\varrho(w)\big) = \rho_s Q_s, & \text{in } \Omega \times (0,T), \\ \theta\dfrac{\partial m(w)}{\partial t} + \nabla \cdot \big(\mathbf{q}m(w)\big) - \nabla \cdot (D\nabla w) = \omega_s \rho_s Q_s & \text{in } \Omega \times (0,T), \end{cases} \tag{1.4}$$

where the unknown functions are now p and w. In the benchmarks, the initial condition and boundary condition of w are directly computed from the corresponding conditions of c. We consider 3 benchmarks, a rotating interface problem and Henry's problem in space dimension 2 and a 3 dimensional saltpool problem. We refer to [9] for a finite element discretization of Problem (1.1) in space dimension 3. An advantage of finite volume methods is that the discrete integrals of the functions $\rho(c)$ and $\rho(c)c$ are numerically accurately preserved. We discuss the mass conservation in Section 3.4.

We then take the heat transfer into consideration. Heat can be recovered from groundwater. Depending on the application, the recovered heat can be used for the production of heat or for power generation. The geothermal heating allows both to replace conventional heating and to produce hot water. We study a coupled system describing the interaction between flow and transport in a porous medium, where the density and the viscosity depend on the concentration of the species being transported, and also on the temperature. We use a model problem proposed in the SEAWAT documentation [10] as a test case. This model problem consists in a two-dimensional cross section of a confined coastal aquifer initially saturated with relatively cold seawater at a temperature of $5°C$. Warmer fresh water with a temperature of $25°C$ is injected into the coastal aquifer along the left boundary to represent the flow from inland areas. The warmer fresh water flows from left to right, where it discharges into a vertical ocean boundary. The ocean boundary is represented with hydrostatic conditions based on the fluid density calculated from seawater salinity at $5°C$. No

flow conditions are assigned to the top and bottom boundaries. Mathematically, we solve a system for the hydraulic water head h, the solute concentration C and the temperature Θ; note that the fluid density ρ and viscosity μ are functions of h, C and Θ. This problem is a simplified representation of what may occur in a coastal carbonate platform.

The outline of this paper is as follows. In Section 2, we introduce the space and time discretization and the generalized finite volume method SUSHI and present the method of mesh refinement. In Section 3, we present our numerical algorithm which is based upon the SUSHI scheme. We present numerical results for 3 test cases: a rotating interface problem and Henry's problem in space dimension 2 and a 3 dimensional saltpool problem. In Section 4, we consider the density driven flow problem coupled with heat transfer and apply a semi-implicit scheme for the time discretization coupled with the SUSHI scheme for the space discretization. We perform simulations and compare our results with the results of SEAWAT. Our results are very close to the results obtained by SEAWAT.

2 Numerical method and adaptive mesh

2.1 The generalized finite volume method SUSHI

In order to present the numerical scheme, we first introduce notations related to the space and time discretization.

Definition 2.1 (Space discretization)**.** Let Ω be a polyhedral open bounded connected subset of $\mathbb{R}^d$ and $\partial\Omega = \overline{\Omega}\backslash\Omega$ its boundary. A discretization of Ω, denoted by $\mathcal{D}$, is defined as the triplet $\mathcal{D} = (\mathcal{M}, \mathcal{E}, \mathcal{P})$, where:

1. $\mathcal{M}$ is a finite family of non empty convex open disjoint subsets of Ω (the "control volumes") such that $\overline{\Omega} = \bigcup_{K\in\mathcal{M}} \overline{K}$. For any $K \in \mathcal{M}$, let $\partial K = \overline{K}\backslash K$ be the boundary of K; we denote by $|K|$ the measure of K and $d(K)$ the diameter of K.

2. $\mathcal{E}$ is a finite family of disjoint subsets of $\overline{\Omega}$ (the "interfaces"), such that, for all $\sigma \in \mathcal{E}$, σ is a nonempty open subset of a hyperplane of $\mathbb{R}^d$ and denote by $|\sigma|$ its measure. We assume that, for all $K \in \mathcal{M}$, there exists a subset $\mathcal{E}_K$ of $\mathcal{E}$ such that $\partial K = \bigcup_{\sigma\in\mathcal{E}_K} \overline{\sigma}$.

3. $\mathcal{P}$ is a family of points of Ω indexed by $\mathcal{M}$, denoted by $\mathcal{P} = (\mathbf{x}_K)_{K\in\mathcal{M}}$, such that for all $K \in \mathcal{M}$, $\mathbf{x}_K \in K$ and K is assumed to be $\mathbf{x}_K$-star-shaped, which means that for all $\mathbf{x} \in K$, the inclusion $[\mathbf{x}_K, \mathbf{x}] \subset K$ holds.

For all $\sigma \in \mathcal{E}$, we denote by $\mathbf{x}_\sigma$ the barycenter of σ. For all $K \in \mathcal{M}$ and $\sigma \in \mathcal{E}_K$, we denote by $D_{K,\sigma}$ the cone with vertex $\mathbf{x}_K$ and basic σ, by $\mathbf{n}_{K,\sigma}$ the unit vector normal to σ outward to K and by $d_{K,\sigma}$ the Euclidean distance between $\mathbf{x}_K$ and the hyperplane including σ. For all $\sigma \in \mathcal{E}$, we define $\mathcal{M}_\sigma = \{K \in \mathcal{M} : \sigma \in \mathcal{E}_K\}$. And we denote by $\mathcal{E}_{int}$ for the ensemble of all the inner edges.

Definition 2.2 (Time discretization)**.** We divide the time interval $[0, T]$ into N equal time steps of length $\delta t = T/N$. Thus $\delta t = t_n - t_{n-1}$ for all $n = 1, ..., N$, where $t_0 = 0$.

In order to present the application of the SUSHI method, we formally integrate the two last equations of (1.4) on the domain $K \times (t_{n-1}, t_n)$ for each $K \in \mathcal{M}$ and $n = 1, ..., N$ to

obtain

$$\begin{aligned}
&\theta \int_K \Big(\varrho(w(\mathbf{x}, t_n)) - \varrho(w(\mathbf{x}, t_{n-1})) \Big)\, d\mathbf{x} \\
&\qquad + \sum_{\sigma \in \mathcal{E}_K} \int_{t_{n-1}}^{t_n} \int_\sigma \mathbf{q} \varrho(w) \cdot \mathbf{n}_{K,\sigma} d\gamma dt = \int_{t_{n-1}}^{t_n} \int_K \rho_s Q_s \; d\mathbf{x} dt, \\
&\theta \int_K \{ m(w(\mathbf{x}, t_n)) - m(w(\mathbf{x}, t_{n-1})) \}\; d\mathbf{x} + \sum_{\sigma \in \mathcal{E}_K} \int_{t_{n-1}}^{t_n} \int_\sigma \mathbf{q} m(w) \cdot \mathbf{n}_{K,\sigma} d\gamma dt \\
&\qquad - \sum_{\sigma \in \mathcal{E}_K} \int_{t_{n-1}}^{t_n} \int_\sigma D \nabla w \cdot \mathbf{n}_{K,\sigma} d\gamma dt = \int_{t_{n-1}}^{t_n} \int_K \; \omega_s \rho_s Q_s \; d\mathbf{x} dt.
\end{aligned} \tag{2.1}$$

We first denote by $F^D_{K,\sigma}(w)$ the numerical flux which approximates the diffusion flux $\int_\sigma -D\nabla w \cdot \mathbf{n}_{K,\sigma} d\gamma$. We recall below formulas which have been derived by [4].

$$F^D_{K,\sigma}(w) = \sum_{\sigma' \in \mathcal{E}_K} A^{\sigma\sigma'}_K (w_K - w_{\sigma'}), \tag{2.2}$$

where the matrices $A^{\sigma\sigma'}_K$, which are symmetric and positive-definite, are defined by

$$A^{\sigma\sigma'}_K = \sum_{\sigma'' \in \mathcal{E}_K} \mathbf{y}^{\sigma''\sigma} \cdot D_{K,\sigma''} \mathbf{y}^{\sigma''\sigma'} \quad \text{where} \quad D_{K,\sigma''} = \int_{V_{K,\sigma''}} D d\mathbf{x}. \tag{2.3}$$

$V_{K,\sigma''}$ is the cone with the vertex point $\mathbf{x}_K$ and the base σ'' with

$$\mathbf{y}^{\sigma\sigma'} = \begin{cases} \dfrac{|\sigma|}{|K|}\mathbf{n}_{K,\sigma} + \dfrac{\sqrt{d}}{d_{K,\sigma}}(1 - \dfrac{|\sigma|}{|K|}\mathbf{n}_{K,\sigma} \cdot (\mathbf{x}_\sigma - \mathbf{x}_K))\mathbf{n}_{K,\sigma} & \text{if} \quad \sigma = \sigma', \\ \dfrac{|\sigma'|}{|K|}\mathbf{n}_{K,\sigma} - \dfrac{\sqrt{d}}{d_{K,\sigma}\,|K|}\,|\sigma'|\,\mathbf{n}_{K,\sigma'} \cdot (\mathbf{x}_\sigma - \mathbf{x}_K)\mathbf{n}_{K,\sigma} & \text{otherwise}, \end{cases} \tag{2.4}$$

where d is the space dimension.

Next we denote by $F^C_{K,\sigma}(p, w)$ which approximates the term $\int_\sigma \mathbf{q} \cdot \mathbf{n}_{K,\sigma} d\gamma$. We apply an idea in [7] and set

$$F^C_{K,\sigma}(p, w) = \frac{k}{\mu}\Big(\sum_{\sigma' \in \mathcal{E}_K} \overline{A^{\sigma\sigma'}_K}(p_K - p_\sigma) + |\sigma| \mathbf{g} \cdot \mathbf{n}_{K,\sigma} \cdot \varrho(w_\sigma) \Big), \tag{2.5}$$

for all $\sigma \in \mathcal{E}_K$, where $\overline{A^{\sigma\sigma'}_K} = \sum_{\sigma'' \in \mathcal{E}_K} \mathbf{y}^{\sigma''\sigma} \cdot \overline{D_{K,\sigma''}} \mathbf{y}^{\sigma''\sigma'}$ with $\overline{D_{K,\sigma''}} = \int_{V_{K,\sigma''}} 1 d\mathbf{x}$. As a result, we have the following approximations

$$\int_\sigma \mathbf{q} \varrho(w) \cdot \mathbf{n}_{K,\sigma} d\gamma \approx F^C_{K,\sigma}(p, w) \varrho(w_\sigma),$$

$$\int_\sigma \mathbf{q} m(w) \cdot \mathbf{n}_{K,\sigma} d\gamma \approx F^C_{K,\sigma}(p, w) m(w_\sigma),$$

which will be applied in section 3.2.

2.2 Adaptive mesh

An essential feature of the generalized finite volume method SUSHI scheme is that it allows to use non-matching volume elements. This permits us to apply an adaptive mesh method combining square or cubic elements of different sizes in the numerical tests. We refine the mesh in regions of strong variations of the unknown function while we merge elements in areas where the unknown function undergoes small variations. The adaptive mesh reduces the number of elements and edges, and economizes CPU time. After each refinement or merge, we calculate the values of discrete unknown functions of next time step on the new mesh.

In many articles, the value of the discrete gradients is often chosen as a refinement criterion. In this work, we introduce a new criterion which is based on the discrete difference of unknowns. The advantages of this method are: (1) it is easy to implement, and (2) we can easily manage the number of unknowns as well as the refinement-remerge areas. Moreover, in some cases, the discrete gradient and discrete difference give the same results, for example in the case where the mesh size is close to uniform in the refinement area.

To this purpose, we define the maximum of the discrete difference of unknowns at the cell center and at its edges: $U_K = \max_{\sigma \in \mathcal{E}_K} |u_K - u_\sigma|$ where u is a chosen unknown. Then we sort all the elements in order of increasing U_K. The element L is added to a list called "refined-list" if $(U_L - \min_{K \in \mathcal{M}} U_K)/(\max_{K \in \mathcal{M}} U_K - \min_{K \in \mathcal{M}} U_K) > \alpha$ where $0 < \alpha < 1$. It means that the "refined list" includes the elements whose unknown undergoes the highest discrete difference. The scalar α controls the amount of refined elements (the length of the refined-list). If $\alpha = 0.75$, around one fourth of the elements of the current mesh will be refined. If α is close to 1, the refined-list is very short. If the element L satisfies $(U_L - \min_{K \in \mathcal{M}} U_K)/(\max_{K \in \mathcal{M}} U_K - \min_{K \in \mathcal{M}} U_K) < \beta$ where $0 < \beta < \alpha$, it is added to the "coarse-list". In a similar way, the scalar β controls the length of the coarse-list. If β tends to 0, the coarse-list becomes empty. Figure 1 demonstrates our statements.

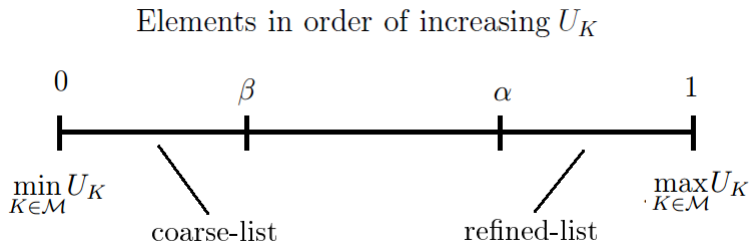

Figure 1: The refined-list and the coarse-list.

We start with a uniform square in space dimension 2 or a uniform cubic mesh in space dimension 3. After each time step, we compute a new coarse-list and a new refined-list. If an element belongs to the refined-list, it is divided into smaller ones: it will be divided into 4 small squares in space dimension 2 or 8 cubes in space dimension 3. If some neighbor elements belong to the coarse-list, they are merged together. We refer to [14] for detailed

interpolation methods and we use linear interpolation to assign values to the new unknowns after each refinement. In practice u corresponds to the salt concentration, except at the end of this paper where u is taken one time as the temperature.

3 Density driven flows in porous media

3.1 Initial condition on p

In system (1.4), when c is known, the second equation is an elliptic equation of p. Thus, we do not need any initial condition for p. We refer to [5] for the discussion of the compatibility relation between the pressure p and the density ρ.

However, in the discretized form of the problem, we will need to impose an initial condition for p, which we do by solving the elliptic equation $\nabla \cdot \big(\mathbf{q}\varrho(w_0)\big) = 0$ together with the given boundary conditions provided that a Dirichlet boundary condition is imposed on a part of the boundary (Henry's problem and the saltpool problem); otherwise the initial pressure would not be uniquely defined.

In the rotating interface problem, due to the Neumann boundary condition on p, there is no uniqueness of the solution p. This leads us to add an extra term $\epsilon\partial p(\mathbf{x},t)/\partial t$ to the second equation of system (1.4) with ϵ small. Therefore the equation for p becomes parabolic so that we have to impose an initial condition; we will suppose that the initial condition is such that $p(\mathbf{x},0) = 0$ at $\mathbf{x}_0 = (0,0)$ and satisfies $\nabla \cdot \big(\mathbf{q}\varrho(w_0)\big) = 0$ for all $\mathbf{x} \in \Omega$ together with the homogenous Neumann boundary condition on $\partial\Omega$. Then the initial pressure is uniquely defined.

3.2 Numerical scheme

We associate with the mesh the following discrete spaces

$$X_{\mathcal{D}} = \{((v_K)_{K\in\mathcal{M}}, (v_\sigma)_{\sigma\in\mathcal{E}}), v_K \in \mathbb{R}, v_\sigma \in \mathbb{R}\}.$$

We first discuss the discretization of the initial condition. As w is a function of c, the initial condition of the scheme for w is computed based on the initial condition of c by

$$w_K^0 = \frac{1}{|K|}\int_K w\big(c_0(\mathbf{x})\big)d\mathbf{x}, \quad w_\sigma^0 = \frac{1}{|\sigma|}\int_\sigma w\big(c_0(\mathbf{x})\big)d\gamma. \tag{3.1}$$

As mentioned in the section 3.1, if $p_0(x)$ is given, we use a similar scheme to obtain the discrete initial condition

$$p_K^0 = \frac{1}{|K|}\int_K p_0(\mathbf{x})d\mathbf{x}, \quad p_\sigma^0 = \frac{1}{|\sigma|}\int_\sigma p_0(\mathbf{x})d\gamma. \tag{3.2}$$

In the rotating interface problem, in Henry's problem and in the saltpool problem, we solve numerically the equations described in the section 3.1 to obtain the discrete initial condition for p in $X_{\mathcal{D}}$.

Next we present a semi-implicit finite volume scheme corresponding to system (1.4), after plugging in the Darcy's law into the 2 last equations. For each $n \in \{1, ..., N\}$:

We suppose that w^{n-1} and w^{n-2} are already known and search for $p^n \in X_D$ such that

$$\begin{cases} \dfrac{\theta|K|}{\delta t}\big(\varrho(w_K^{n-1}) - \varrho(w_K^{n-2})\big) \\ \qquad\qquad + \displaystyle\sum_{\sigma\in\mathcal{E}_K} \Big\{F_{K,\sigma}^C(p^n, w^{n-1}) \cdot \varrho(w_\sigma^{n-1})\Big\} = \dfrac{(Q_\rho)_K^n}{\delta t} & \text{for all } K \in \mathcal{M}, \quad (3.3a) \\ \displaystyle\sum_{K\in\mathcal{M}_\sigma} \Big\{F_{K,\sigma}^C(p^n, w^{n-1}) \cdot \varrho(w_\sigma^{n-1})\Big\} = 0 & \text{for all } \sigma \in \mathcal{E}_{int}, \quad (3.3b) \\ F_{K,\sigma}^C(p^n, w^{n-1}) = |\sigma|\overline{q}_N(\mathbf{x}_\sigma, t_n) & \text{for all } \mathbf{x}_\sigma \in \partial\Omega_N^p, \quad (3.3c) \\ p_\sigma^n = p_D(\mathbf{x}_\sigma, t_n) & \text{for all } \mathbf{x}_\sigma \in \partial\Omega_D^p. \quad (3.3d) \end{cases}$$

Then, knowing p^n and w^{n-1}, we search for $w^n \in X_D$ such that

$$\begin{cases} \dfrac{\theta|K|}{\delta t}\big(m(w_K^n) - m(w_K^{n-1})\big) + \displaystyle\sum_{\sigma\in\mathcal{E}_K} F_{K,\sigma}^D(w^n) \\ \qquad\qquad + \displaystyle\sum_{\sigma\in\mathcal{E}_K} F_{K,\sigma}^C(p^n, w^{n-1}) \cdot m(\tilde{w}_{K,\sigma}^n) = \dfrac{Q_K^n}{\delta t} & \text{for all } K \in \mathcal{M}, \quad (3.4a) \\ \displaystyle\sum_{K\in\mathcal{M}_\sigma} \Big\{F_{K,\sigma}^D(w^n) + F_{K,\sigma}^C\big(p^n, w^{n-1}\big) \cdot m(\tilde{w}_{K,\sigma}^n)\Big\} = 0 & \text{for all } \sigma \in \mathcal{E}_{int}, \quad (3.4b) \\ F_{K,\sigma}^D(w^n) = -|\sigma| D(\mathbf{x}_\sigma, t_n) \dfrac{\partial w}{\partial c}(\mathbf{x}_\sigma, t_n) \cdot \overline{c}_N(\mathbf{x}_\sigma, t_n) & \text{for all } \mathbf{x}_\sigma \in \partial\Omega_N^c, \quad (3.4c) \\ w_\sigma = w\big(c_D(\mathbf{x}_\sigma, t_n)\big) & \text{for all } \mathbf{x}_\sigma \in \partial\Omega_D^c. \quad (3.4d) \end{cases}$$

where $(Q_\rho)_K^n = \int_{t^{n-1}}^{t^n} \int_K \rho_s Q_s d\mathbf{x}dt$ and $Q_K^n = \int_{t^{n-1}}^{t^n} \int_K \omega_s \rho_s Q_s d\mathbf{x}dt$. We denote by $\partial\Omega_D^p$ and $\partial\Omega_D^c$ the parts of the boundary corresponding to the Dirichlet boundary conditions and by $\partial\Omega_N^p$ and $\partial\Omega_N^c$ the parts of the boundary corresponding to the Neumann boundary conditions for the pressure p and the concentration c respectively. When $n = 1$, we omit the term $\varrho(w_K^{n-1}) - \varrho(w_K^{n-2})$ in the equation (3.3a). The two equations (3.3b) and (3.4b) come from the local conservation of the discrete fluxes on the interior edges. We apply a centered scheme for the convection term in (3.3) and an upwind scheme for the convection term in (3.4). More precisely, we define $\tilde{w}_{K,\sigma}$ according to the upwind scheme

$$m(\tilde{w}_{K,\sigma}^n) = \begin{cases} m(w_K^n) & \text{if} \quad F_{K,\sigma}^C(p^n, w^{n-1}) > 0 \\ m(w_\sigma^n) & \text{otherwise.} \end{cases}$$

Moreover, in the discrete equation (3.4), $m(w^n)$ is a nonlinear function of unknown w^n. We apply Newton's method to calculate w^n.

3.3 The rotating interface problem

The rotating interface problem involves zero source terms: $Q_s = 0$ together with the boundary conditions,

$$\begin{cases} \dfrac{\partial c}{\partial n} = 0 & \text{on } \partial\Omega \times [0,T] \\ \mathbf{q} \cdot \mathbf{n} = 0 & \text{on } \partial\Omega \times [0,T] \end{cases} \tag{3.5}$$

where $\Omega = (0,100) \times (0,100)\ m^2$ and $T = 500$ days.

As already mentioned above, a technical problem is that if p is a solution, $p+\bar{p}$ is a solution as well, with $\bar{p}$ an arbitrary constant. This leads us to transform the elliptic equation for p into a parabolic equation by adding the extra term $\epsilon \partial p(\mathbf{x},t)/\partial t$ which makes the model slightly compressible,

$$\epsilon \frac{\partial p}{\partial t} + \theta \frac{\partial \varrho(w)}{\partial t} + \nabla \cdot (\mathbf{q}\varrho(w)) = 0. \tag{3.6}$$

Then the discretized form of the equation for p is given by:

$$\frac{\epsilon|K|}{\delta t}(p_K^n - p_K^{n-1}) + \frac{\theta|K|}{\delta t}\big(\varrho(w_K^{n-1}) - \varrho(w_K^{n-2})\big) + \sum_{\sigma \in \mathcal{E}_K} F_{K,\sigma}^C\big(p^n, m(w^{n-1})\big)\varrho(w_{K,\sigma}^{n-1}) = 0. \tag{3.7}$$

The initial concentration is given by $c(\mathbf{x},0) = 0$ if $\mathbf{x}$ belongs to the right half domain and $c(\mathbf{x},0) = 1$ otherwise. The initial condtion for p has been discussed in section 3.1. The parameter values are defined in Table 1. Note that with the homogenous Neumann boundary condition (3.5), the conservation of mass holds as indicated in (3.9). The conservation of mass is discussed in the subsection 3.4 below.

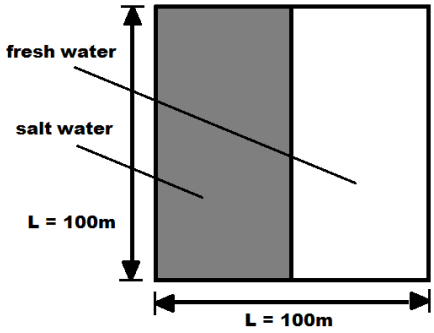

Figure 2: The initial condition for the rotating interface problem.

Symbol	Value	Unit
k	3.1×10^{-12}	m^2
D	3.3×10^{-6}	m^2/s
g	9.81	m/s^2
θ	0.5	-
μ	10^{-3}	$kg/(m \cdot s)$
ρ_0	10^3	kg/m^3
$\bar{a}$	0.3	-
ϵ	10^{-5}	-

Table 1: Parameters for the rotating interface problem.

Because of the gravity, the salt water, which is heavier, diffuses towards the bottom; meanwhile the pure water, which is lighter, diffuses towards the top. Therefore, the interface slowly evolves from a vertical to a horizontal line. After about 300 days, the fluid is in equilibrium and the motion stops. One can observe the movement of the interface in the figures 3 and 4. Figure 3 shows the flux field $\mathbf{q}$ of the problem at the initial time and at time $t = 200$ days while the second one shows the time evolution of the concentration. The refined elements are essentially located in the neighbourhood of the interface and follow it as it moves.

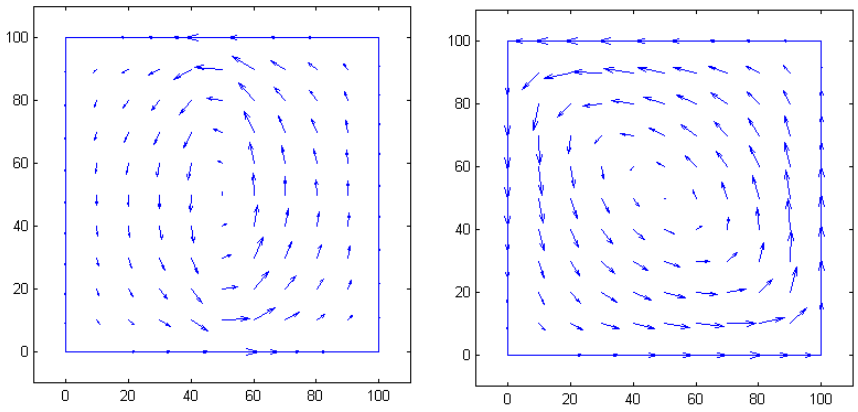

Figure 3: The flux field **q** of the rotating interface problem.

In the simulation, we start with a very coarse discretization mesh with 5×5 square elements. An adaptive mesh is applied at each time step, taking into account the variations of the concentration c. We present the numerical results of the concentration in Figure 4. At the beginning, because the mesh is coarse, we choose $\alpha = 0.75$ to create more refined elements. Then we choose $\beta = 0.2$ to make a balance between refinement and derefinement. At $t = 50$ days, the number of elements is large enough, we choose again $\alpha = 0.85$ to reduce the number of volume elements to be refined and β is also decreased to $\beta = 0.1$. From $t = 250$ to the end, the evolution is slow, so that we choose $\alpha = 0.95$ and $\beta \simeq 0$. Table 2 shows the number of volume elements of the adaptive mesh at various times. At the beginning, the adaptive mesh has a small number of elements. At the end, the mesh is approximately a uniform mesh of 40×40. In Figure 5 we compare the CPU times with different meshes, namely three uniform meshes with respectively 100 (10×10), 400 (20×20) and 1600 (40×40) volume elements and an adaptive mesh.

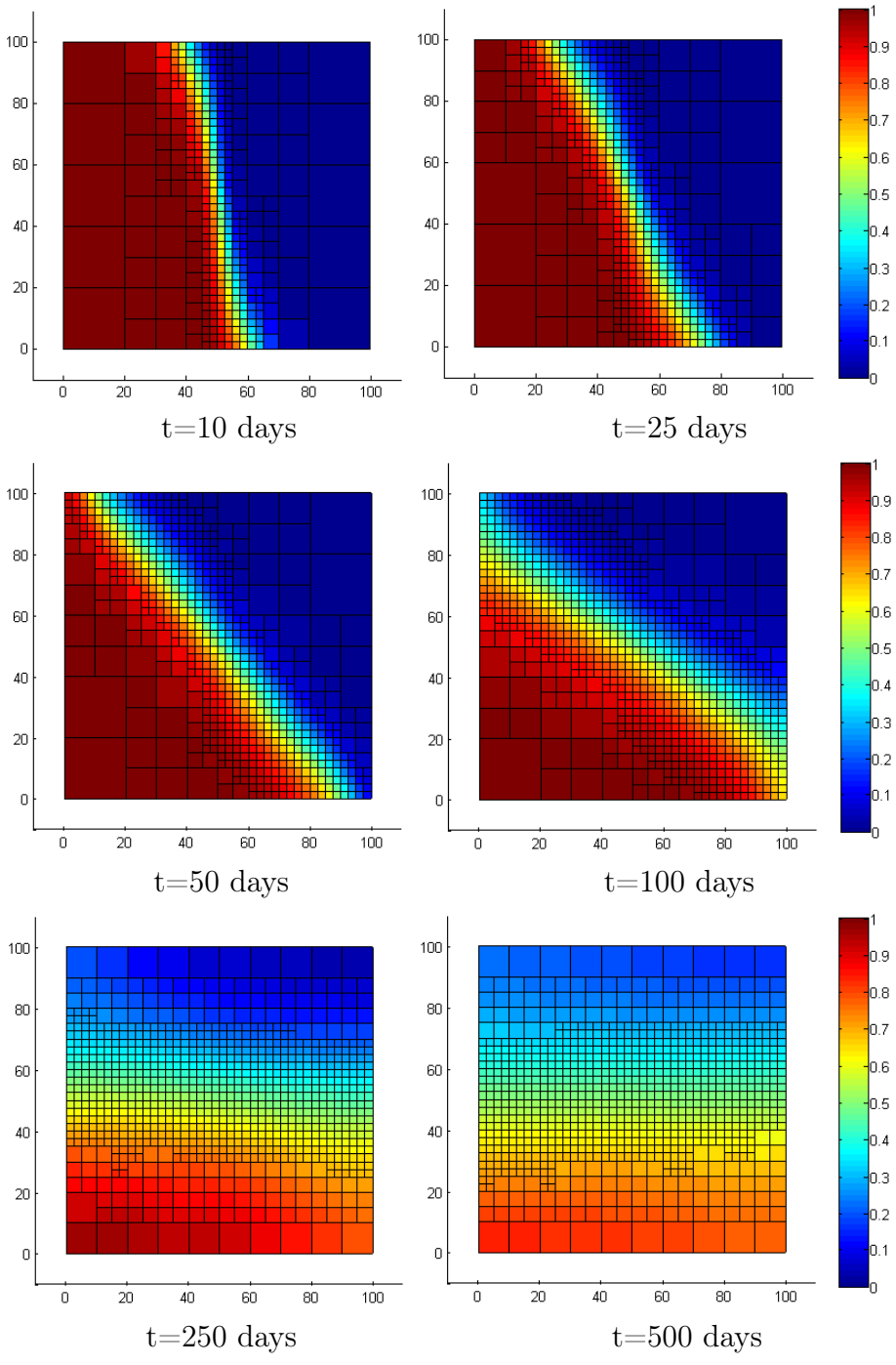

Figure 4: Time evolution of the concentration using an adaptive mesh.

Time	NoE	NoU
t=0 days	120	420
t=10 days	355	1123
t=20 days	499	1567
t=30 days	583	1825
t=50 days	597	2171
t=100 days	934	2882
t=200 days	1192	3660
t=300 days	1309	4013
t=500 days	1378	4221

Table 2: Number of volume elements (NoE) and Number of unknowns (NoU) in the rotating interface problem using an adaptive mesh.

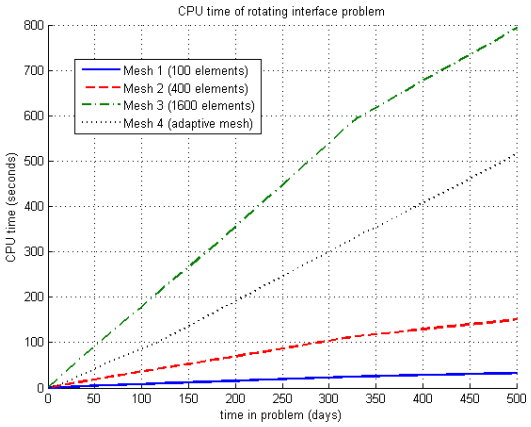

Figure 5: CPU time in the rotating interface problem using different meshes.

3.4 Mass conservation

In this subsection we discuss the conservation of mass. We first check the mass conservation in the partial differential equation system. For each t, we integrate the transport equation (1.1c) on $\Omega \times (0,t)$ in the case that $Q_s = 0$:

$$\int_\Omega \theta\big(\rho(c(\mathbf{x},t))c(\mathbf{x},t) - \rho(c_0(\mathbf{x}))c_0(\mathbf{x})\big)d\mathbf{x} + \int_0^t \int_\Omega \nabla\cdot(\mathbf{q}\rho(c(\mathbf{x},\tau))c(x,\tau))d\mathbf{x}d\tau - \int_0^t \int_\Omega \nabla\cdot(D\nabla w(c(\mathbf{x},\tau)))d\mathbf{x}d\tau = 0,$$

which yields

$$\theta\Big(\int_\Omega \rho(c(\mathbf{x},t))c(\mathbf{x},t)d\mathbf{x} - \int_\Omega \rho(c_0(\mathbf{x}))c_0(\mathbf{x})d\mathbf{x}\Big) = -\int_0^t \int_{\partial\Omega} \rho(c(\mathbf{x},\tau))c(\mathbf{x},\tau)\mathbf{q}\cdot\mathbf{n}\ d\gamma d\tau + \int_0^t \int_{\partial\Omega} D\rho(c(\mathbf{x},\tau))\nabla c\cdot\mathbf{n}\ d\gamma d\tau. \tag{3.8}$$

We recall that that $\mathbf{q}\cdot\mathbf{n} = 0$ and $\partial c/\partial\mathbf{n} = 0$ on $\partial\Omega$, which we substitute in (3.8) to deduce that

$$\int_\Omega \rho(c(\mathbf{x},t))c(\mathbf{x},t)d\mathbf{x} = \int_\Omega \rho(c_0(\mathbf{x}))c_0(\mathbf{x})d\mathbf{x}.$$

Thus the system possesses the mass conservation property. Next, we check the mass is also conserved by the numerical scheme. We add up the semi-implicit discrete equations (3.4) on all control volumes, and setting $Q = 0$, we obtain:

$$\sum_{K\in\mathcal{M}} \theta|K|\big(m(w_K^n) - m(w_K^{n-1})\big) + \delta t \sum_{K\in\mathcal{M}}\sum_{\sigma\in\mathcal{E}_K} \Big(F_{K,\sigma}^D(w^n) + F_{K,\sigma}^C\big(p^n, m(w^{n-1})\big)m(w^n)\Big) = 0.$$

We define the total mass at the time $t_n = n\delta t$ by $\sum_{K\in\mathcal{M}} |K| m(w_K^n)$. Using the local conservation of the discrete fluxes on the interior edges (3.4) and the homogenous Neumann boundary condition, we deduce that:

$$\sum_{K\in\mathcal{M}} |K| m(w_K^n) = \sum_{K\in\mathcal{M}} |K| m(w_K^0), \tag{3.9}$$

which expresses the fact that in our algorithm, the mass is conserved. We check in Table 3 that, in the simulation, the mass is indeed conserved.

Time (days)	**Mass**	**Time (days)**	**Mass**
$t = 0$	6.5×10^6		
$t = 10$	$6.500000000000002 \times 10^6$	$t = 100$	$6.499999999999990 \times 10^6$
$t = 20$	$6.500000000000004 \times 10^6$	$t = 200$	$6.499999999999996 \times 10^6$
$t = 30$	$6.499999999999998 \times 10^6$	$t = 300$	$6.499999999999975 \times 10^6$
$t = 50$	$6.500000000000006 \times 10^6$	$t = 500$	$6.499999999999961 \times 10^6$

Table 3: Total mass obtained by the generalized finite volume method SUSHI.

3.5 Henry's problem

Henry's problem describes the advance of a salt water front in a confined aquifer which is initially charged with fresh water. Henry developed a solution method to compute the steady-state distribution of the solute. He applied the Boussinesq approximation, which involves a stream function. Henry derived analytical expressions for the stream function and the concentration in the form of a Fourier series; the resulting algebraic equations for the determination of the Fourier coefficients must be obtained numerically. The 'mystery' of Henry's problem is that no numerical model so far has been able to closely reproduce his semi-analytical solution. Nevertheless, because of the absence of other non numerical solution for this kind of nonlinear problems, Henry's problem has become one of the standard tests for variable density groundwater models.

Mathematically, Henry's problem is defined as System (1.1) in the rectangle Ω together with zero source term $Q_s = 0$ and the initial conditions, such that $c(\mathbf{x}, 0) = 0$ and that the pressure $p(\mathbf{x}, 0)$ satisfies $\nabla \cdot \big(\mathbf{q}\varrho(w(\mathbf{x}, 0))\big) = 0$ for all $\mathbf{x} \in \Omega$; and the boundary conditions

$$\begin{cases} c = 0 & \text{on } \Gamma_2 \times (0,T), \\ c = 1 & \text{on } \Gamma_3^b \times (0,T), \\ \dfrac{\partial c}{\partial n} = 0 & \text{on } (\Gamma_1 \cup \Gamma_4 \cup \Gamma_3^h) \times (0,T), \\ p = \rho_0 |\mathbf{g}|(\alpha(1-y) - y) & \text{on } \Gamma_3 \times (0,T), \\ \mathbf{q}\cdot\mathbf{n} = 0 & \text{on } (\Gamma_1 \cup \Gamma_4) \times (0,T), \\ \mathbf{q}\cdot\mathbf{n} = q_0 & \text{on } \Gamma_2 \times (0,T), \end{cases} \tag{3.10}$$

where $\Gamma_3 = \Gamma_3^h \cup \Gamma_3^b$ and y is y-coordinate. Figure 6 shows the configuration of the boundary conditions. We perform the numerical tests on the space domain $\Omega = (0,1) \times (0,1)\ m^2$, with $T = 0.05$ day. The parameters are given in Table 4.

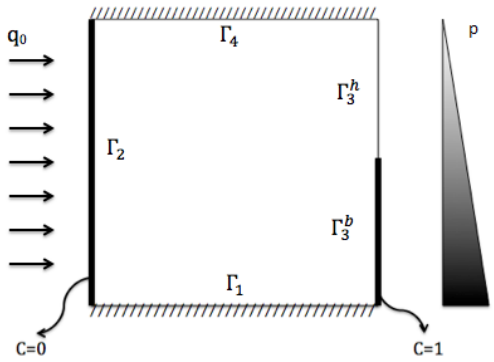

Figure 6: The boundary conditions for Henry's problem.

Symbol	Value	Unit
k	1.02×10^{-9}	m^2
D	6.6×10^{-6}	m^2/s
g	9.81	m/s^2
θ	0.3	-
μ	10^{-3}	$kg/(m \cdot s)$
ρ_0	10^3	$kg \cdot m^3$
$\bar{a}$	0.025	-
q_0	-6.6×10^{-5}	m/d

Table 4: Parameters for Henry's problem.

The simulations in Figure 8 describe the intrusion of salt water in a confined aquifer. The salt water enters from the right-hand-side, while the fresh water, of density ρ_0, flows in from the left-hand-side at a constant rate. Therefore, the concentration in the area near the coastal side increases in time. At first the interface between the fresh and the salt water coming from the right-bottom corner has a large slope (left figure in Figure 7), which slowly decreases in time as the salt concentration enters into the domain (right figure in Figure 7).

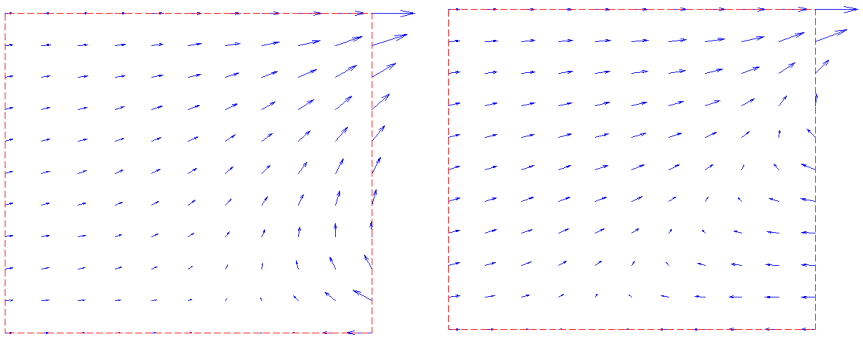

Figure 7: The flux field $\mathbf{q}$ at initial time and final time for Henry's problem.

The variation of the concentration c stays in a region around the boundary $x = 1$, i.e. Γ_3. We refine the mesh according to the variation of c and choose $\alpha = 0.8$ to make the refine-list long enough and set $\beta = 0.15$ to make the process stable. Table 5 presents the number of elements of the adaptive mesh at various times, which is smaller than the number of elements of the uniform mesh 40×40. In the adaptive mesh, the smallest volume elements have the same diameter as the volume elements in the uniform mesh 40×40. The number of elements is one of the reasons why the CPU time is smaller than the CPU time corresponding to the uniform mesh 40×40. The evolutions of the CPU times in different meshes are shown in

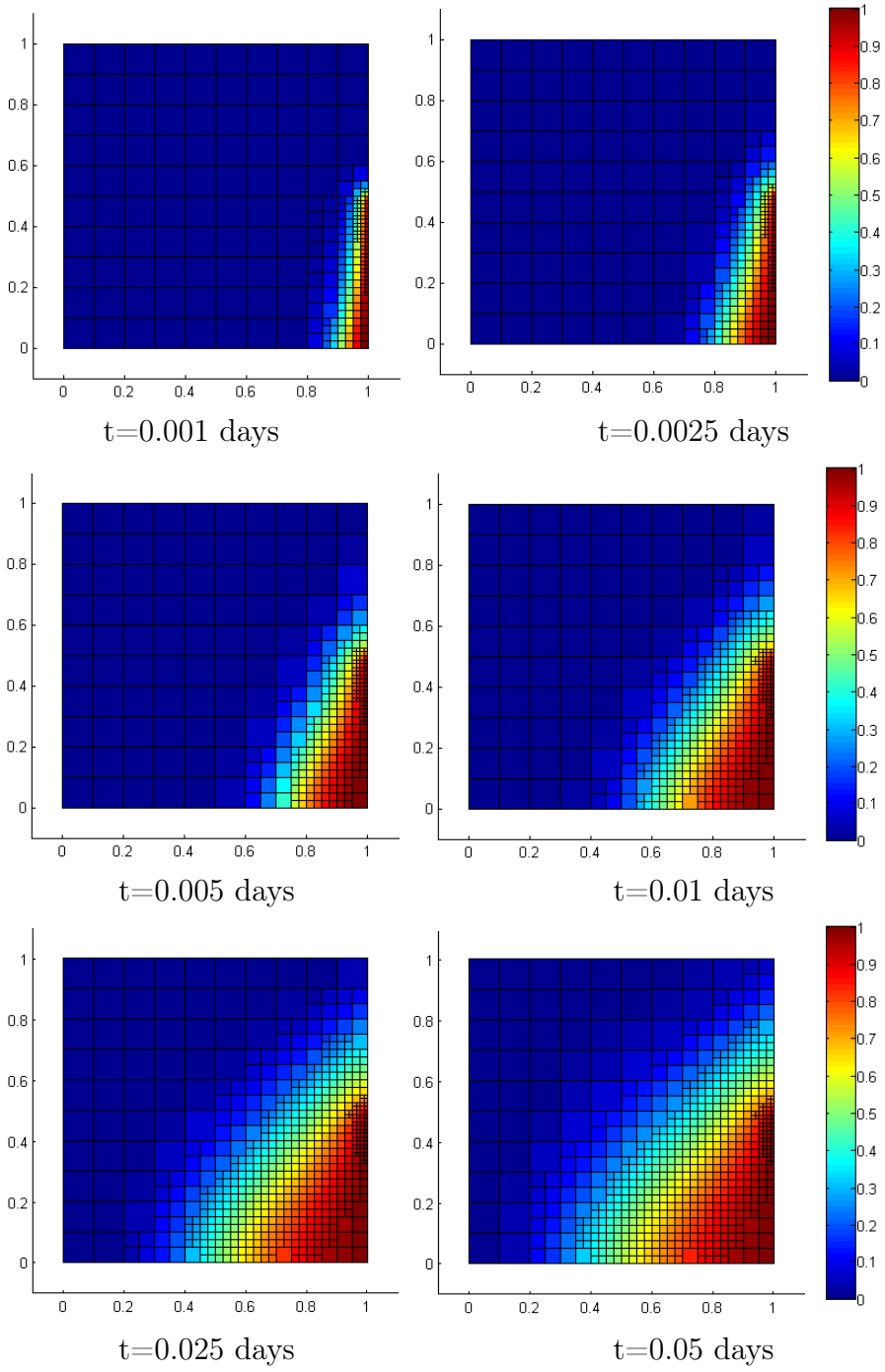

Figure 8: Time evolution of the concentration in Henry's problem using an adaptive mesh.

Figure 9. As a conclusion, when using the same precision over the high variation region, we save CPU time by using an adaptive mesh, especially in the case of Henry's problem.

Time	NoE	NoU
t=0 days	120	420
t=0.001 days	262	844
t=0.002 days	307	983
t=0.003 days	328	1046
t=0.005 days	331	1053
t=0.01 days	469	1477
t=0.02 days	586	1834
t=0.03 days	649	2025
t=0.05 days	673	2099

Table 5: Number of volume elements (NoE) and number of unknowns (NoU) in Henry's problem using an adaptive mesh.

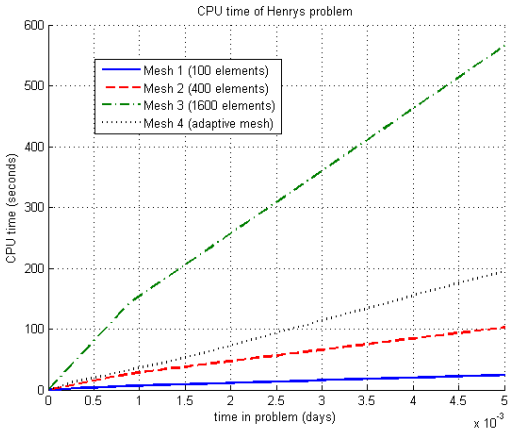

Figure 9: CPU times in Henry's problem using different meshes.

3.6 The saltpool problem

We present below a numerical test in space dimension 3, the saltpool problem, which is studied in [9] and [11]. We consider a $0.2 \times 0.2 \times 0.2\ m^3$ cube with fresh water being injected on top of the domain while the bottom is full of salt water. Initial conditions are such that freshwater lies over saltwater with a $0.008\ m$ wide transition zone centered at $z_m = 0.06\ m$. In the transition zone, the mass fraction varies linearly from $c = 0$ to $c = 1$, that is

$$c(x, y, z, 0) = \begin{cases} 1, & \text{if } z \leq z_m - 0.008/2, \\ \frac{1}{2} - (z - z_m)/0.008, & \text{if } z_m - 0.008/2 < z < z_m + 0.008/2, \\ 0, & \text{if } z \geq z_m + 0.008/2. \end{cases} \tag{3.11}$$

The source term is such that $Q_s = 0$. Boundary conditions for the flow equation (1.1b) are modeled by an inlet normal flux Neumann condition in the inlet area $a_1 = 0.01 \times 0.01\ m^2$, and a Dirichlet freshwater piezometric head condition corresponding to a pressure value zero at the outlet $a_2 = 0.01 \times 0.01\ m^2$. On all other parts of the boundary, no flow boundary conditions are imposed. As for the transport equation (1.1c), we impose a homogenous Dirichlet boundary condition on the inlet area a_1, while we impose a homogenous Neumann boundary condition on $\Gamma \setminus a_1$. In summary, the boundary conditions for the saltpool problem are given by

$$\begin{cases} \mathbf{q} = -Q, & \text{on } a_1 \\ p = 0, & \text{on } a_2 \\ \dfrac{\partial p}{\partial n} = 0, & \text{on } \Gamma \setminus \{a_1 \cup a_2\} \\ c = 0, & \text{on } a_1 \\ \dfrac{\partial c}{\partial n} = 0, & \text{on } \Gamma \setminus a_1 \end{cases} \tag{3.12}$$

For the dispersion-diffusion tensor in (1.1c), we apply the Scheidegger's dispersion model

$$\mathbf{D}(\mathbf{q}) = \theta D\mathbf{I} + (\alpha_L - \alpha_T)\frac{\mathbf{q}^T \otimes \mathbf{q}}{|\mathbf{q}|} + \alpha_T|\mathbf{q}|\mathbf{I}, \tag{3.13}$$

where α_L and α_T are the longitudinal and transverse dispersivity of the isotropic porous medium, respectively. And we compute the numerical flux $\mathbf{q}_K^n$ in element K as follows

$$\mathbf{q}_K^n = \frac{1}{2}\sum_{\sigma\in\mathcal{E}_K}\frac{1}{|\sigma|}F_{K,\sigma}^C(p^n, w^{n-1})\mathbf{n}_{K,\sigma} \quad \text{for all } K \in \mathcal{M}.$$

In this test case, we perform a simulation corresponding to test case 1 of the article by K. Johannesen et al. [9]. The parameters are presented in Table 6. For the discretization, we start with a coarse mesh $5 \times 5 \times 5$ elements. We use a fixed time step $\delta t = 100$ seconds. The regions around the inlet and outlet as well as at the interface are refined at time step $n = 0$ to capture the boundary effect. Figure 11 shows the time evolution of the process while Figure 12 shows the outlet concentration obtained by means of (i) our simulation; (ii) the simulation of [9]; (iii) the real experiment. In the first period, our result is very close to the experimental result. In the time interval $[1000, 4000]$ seconds, it is a little further from the experimental curve but it is slightly better than the result from [9]. In the last period, the result from [9] is closer to the experimental result than our result.

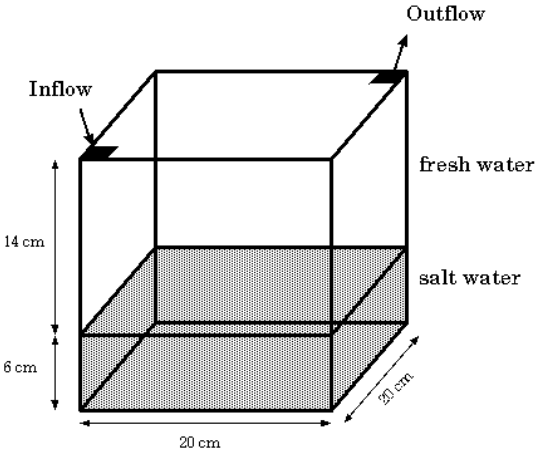

Figure 10: The geometry of the saltpool problem.

Symbol	Value	Unit
k	1.19×10^{-9}	m^2
D	1.06×10^{-9}	m^2/s
g	9.81	m/s^2
θ	0.357	-
μ	1.002×10^{-3}	$kg/(m \cdot s)$
ρ_0	998.2	kg/m^3
$\bar{a}$	0.0076	-
α_L	4.3×10^{-5}	m
α_T	1.2×10^{-3}	m
Q	1.89×10^{-6}	m^3/s

Table 6: Parameters in the saltpool problem.

4 Density driven flow coupled with heat transfer

In this section, we pursue the study of Section 3 on the interaction between flow and transport in porous medium and we take heat transfer into account. The model problem is proposed in the SEAWAT documentation [10].

The SEAWAT code is a computer program for the simulation of a multi-species solute and heat transport [10]. It combines the software codes MODFLOW and MT3DMS which solve

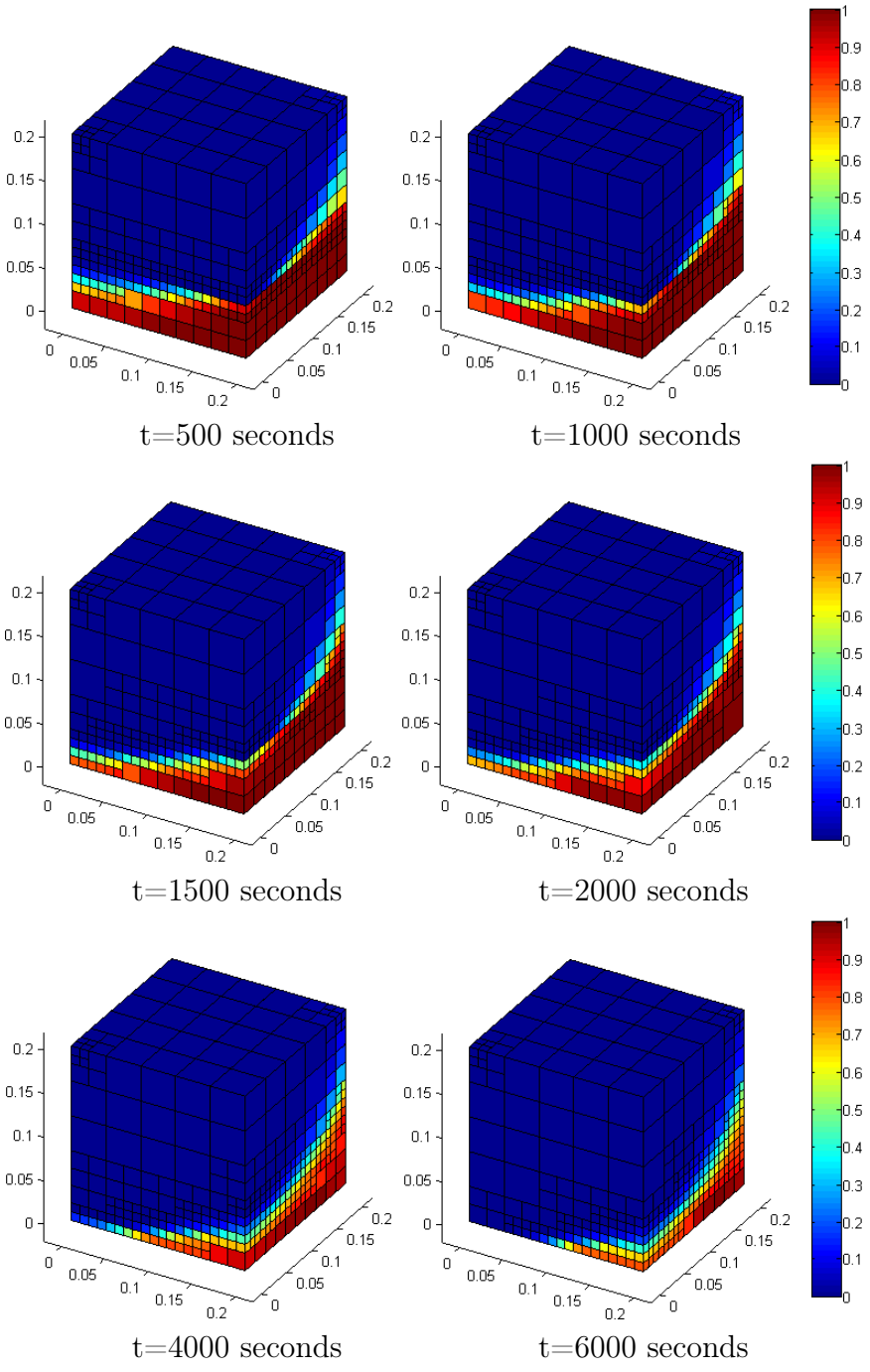

Figure 11: Time evolution of the saltpool problem using an adaptive mesh.

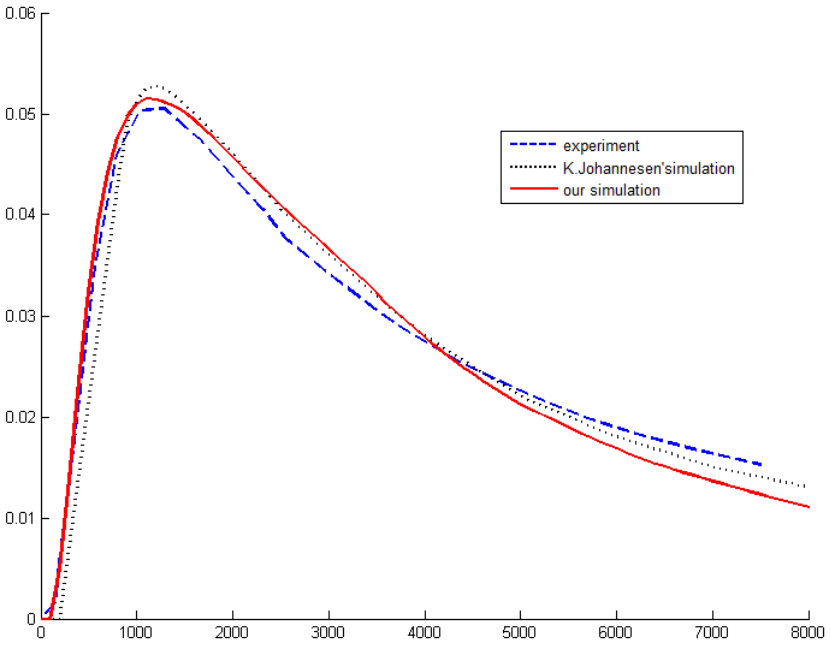

Figure 12: Outlet concentration of the saltpool problem.

the flow and the solute-transport equations respectively. The coupling between flow and transport is performed through a synchronous time-stepping approach that cycles between MODFLOW solutions of the flow equation and MT3DMS solutions of the transport equation. SEAWAT includes both explicit and implicit methods for coupling the flow and the solute-transport equations. With the explicit method, a lagged approach is used for assigning fluid densities in the flow equation. With the implicit coupling method, solutions of the flow and transport equations are repeated interactively solved, and concentrations and densities are updated within each time-step until the maximum difference in fluid density at each single cell for consecutive iterations is less than a user-specified value. As for the numerical methods, SEAWAT uses finite differences for solving the variable-density flow equations. The numerical methods used by the MT3DMS program to simulate solute transport in a constant-density flow field are directly used in SEAWAT to simulate the solute transport in a variable-density flow field.

Both MODFLOW and MT3DMS use cell-centered grids. In this formulation, the dependent variables obtained in the finite-difference solution represent average values (assumed to be given at the cell center) for the respective cells. The same block-centered grid is used by SEAWAT, MODFLOW and MT3DMS.

We propose a uniform code using the generalized finite volume method SUSHI. The structure is much simpler since we deal with a single code instead of two codes which are coupled with each other. We refer to [2] for the study of a related problem by means of a Voronoi box based finite volume method. We apply mesh refinement and show the results of three test cases. Our results are very close to those obtained by SEAWAT.

4.1 Partial differential equation system

4.1.1 Variable density groundwater equation

We consider a system of equations presented in SEAWAT and present below the case of a single species. The space domain is given by the rectangle $\Omega = (0, L) \times (0, H)$. We consider the following form of the variable density groundwater flow equation

$$S_s \rho \frac{\partial h}{\partial t} + \theta \frac{\partial \rho}{\partial C} \frac{\partial C}{\partial t} + \nabla \cdot (\mathbf{q}\rho) = q_s \rho_s \quad \text{in } \Omega \times (0, T), \tag{4.1}$$

where h $[m]$ is the equivalent fresh water head, S_s $[1/m]$ is the specific storage, defined as the water volume released from the storage per unit decline of h, $\rho = \rho(h, C, \Theta)$ $[kg/m^3]$ is the fluid density, θ is the porosity, q_s $[d^{-1}]$ is a source or sink of the fluid with density ρ_s. Equation (4.1) is a generalized form of equation (1.1b). The velocity $\mathbf{q}$ $[m/d]$ is given by Darcy's law:

$$\mathbf{q}(h, \mu, \rho) = -\frac{\mu_0}{\mu} \mathbf{K}_0 \Big(\nabla h + \frac{\rho - \rho_0}{\rho_0} \nabla z \Big), \tag{4.2}$$

where μ $[kg/(m \cdot s)]$ is the dynamic viscosity and μ_0 is a reference viscosity, ρ_0 is the density when the fluid is at the reference concentration C_0 $[kg/m^3]$ and the reference temperature Θ_0 $[^\circ C]$. $\mathbf{K}_0$ $[m/d]$ is the hydraulic conductivity tensor and z $[m]$ is the elevation, such that $\nabla z = (0, 1)^{\mathrm{T}}$.

4.1.2 The fluid density ρ in equation (4.1)

For the transport of the solute species, where the concentration of the species can affect the fluid density, Hughes and Sanford [8] have implemented the following equation of state

$$\rho(h, C, \Theta) = \rho_0 + \frac{\partial \rho}{\partial C}(C - C_0) + \frac{\partial \rho}{\partial \Theta}(\Theta - \Theta_0) + \frac{\partial \rho}{\partial P}(P - P_0).$$

We reformulated here the term $\dfrac{\partial \rho}{\partial P}(P - P_0)$ by using the height of a water column l of density ρ_0. The variable l, which can be thought of as the pressure head in terms of the reference density, is related to the pressure by

$$P = l \rho_0 g,$$

where $l = h - z$. After some simple rearrangements, we can thus rewrite the formula for the fluid density as a function of the concentration, the temperature and the hydraulic head as

$$\rho(h, C, \Theta) = \rho_0 + \frac{\partial \rho}{\partial C}(C - C_0) + \frac{\partial \rho}{\partial \Theta}(\Theta - \Theta_0) + \frac{\partial \rho}{\partial l}(h - h_0). \tag{4.3}$$

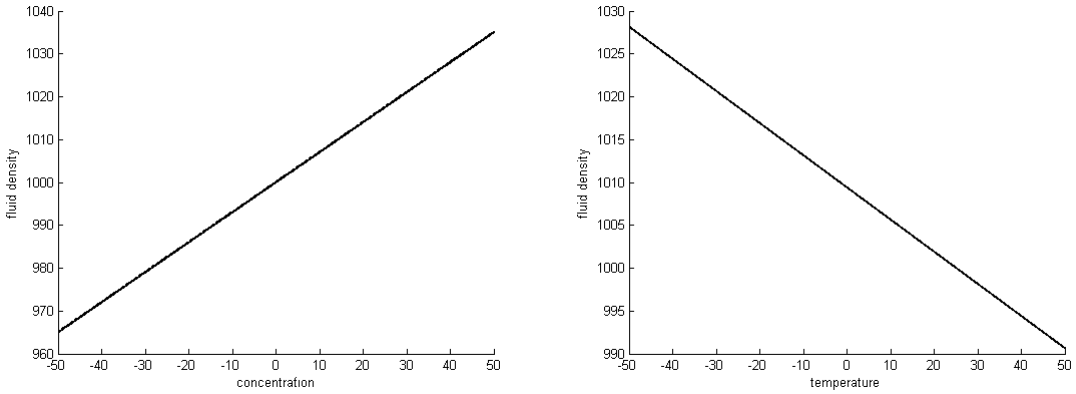

(a) profile of $\rho(0, C, 25)$ (b) profile of $\rho(0, 0, \Theta)$

Figure 13: The fluid density $\rho(C, \Theta, h)$. The parameters are given in Table 7.

4.1.3 The fluid viscosity μ in equation (4.1)

The dynamic viscosity is considered to be a function of temperature and solute concentration, which is a typical approach in [3]; we neglect the dependence of the viscosity on the fluid pressure. A general equation for representing the fluid viscosity as a function of concentration and temperature is given by

$$\mu(C, \Theta) = \mu_0 + \frac{\partial \mu}{\partial C}(C - C_0) + \frac{\partial \mu}{\partial \Theta}(\Theta - \Theta_0).$$

On a number of temperature ranges, the linear approximation does not adequately represent the effect of temperature on the dynamic viscosity. For this reason, an alternative equation for the dynamic viscosity has been implemented, namely

$$\mu(C, \Theta) = \frac{\partial \mu}{\partial C}(C - C_0) + \mu_\Theta(\Theta).$$

There are many options for representing $\mu_\Theta(\Theta)$ as a function of temperature. Here we use the following viscosity and temperature relation

$$\mu_\Theta(\Theta) = A_1 \cdot A_2^{\left(\frac{A_3}{\Theta + A_4}\right)},$$

where the values A_1, A_2, A_3 and A_4 are positive constants (cf. C.I. Voss [13]). As a result we obtain the following formula for the dynamic viscosity

$$\mu(C, \Theta) = \frac{\partial \mu}{\partial C}(C - C_0) + A_1 \cdot A_2^{\left(\frac{A_3}{\Theta + A_4}\right)}. \tag{4.4}$$

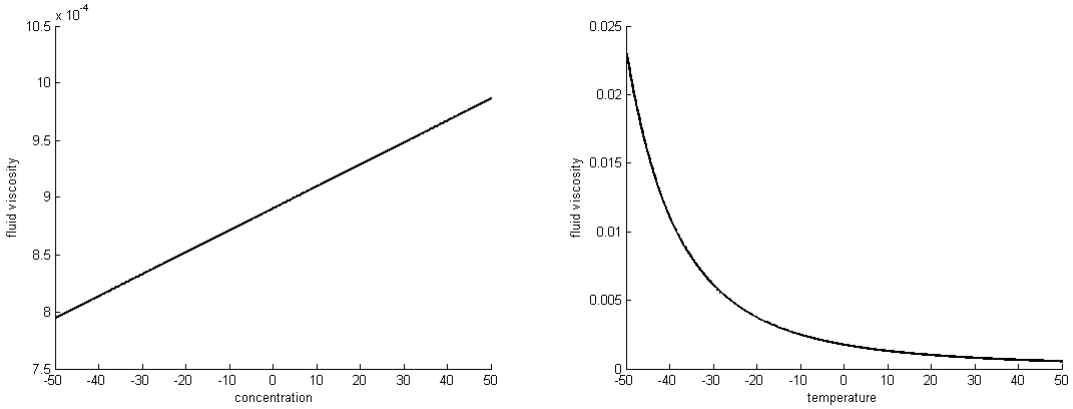

(a) profile of $\mu(C, 25)$ (b) profile of $\mu(0, \Theta)$

Figure 14: The fluid viscosity $\mu(C, \Theta)$. The parameters are given in Table 7.

4.1.4 The solute transport equation and the heat transport equation

The equation for solute transport in groundwater is an advection-dispersion equation. A general form is given by

$$(1 + \frac{\rho_b K_d^C}{\theta})\frac{\partial(\theta C)}{\partial t} + \nabla \cdot (\mathbf{q}C) - \nabla \cdot \Big((\theta D_m^C + \mathbf{a} \cdot \mathbf{q})\nabla C\Big) = q_s C_s \quad \text{in } \Omega \times (0, T), \tag{4.5}$$

where ρ_b $[kg/m^3]$ is the bulk density, K_d^C $[m^3/kg]$ is the distribution coefficient for salinity, D_m^C $[m^2/d]$ is the diffusion coefficient and $\mathbf{a}$ $[m]$ is the dispersivity tensor. We remark that the dispersion tensor is defined as

$$\mathbf{a} \cdot \mathbf{q} := (a_L - a_T)\frac{\mathbf{q} \otimes \mathbf{q}}{|\mathbf{q}|} + a_T|\mathbf{q}|\mathbf{I}. \tag{4.6}$$

Next we present a possible form for the heat transport equation, which was proposed by Thorne et al. [12] to highlight the similarity with the solute transport equation

$$(1 + \frac{\rho_b K_d^\Theta}{\theta})\frac{\partial(\theta\Theta)}{\partial t} + \nabla \cdot (\mathbf{q}\Theta) - \nabla \cdot \Big((\theta D_m^\Theta + \mathbf{a} \cdot \mathbf{q})\nabla\Theta\Big) = q_s \Theta_s \quad \text{in } \Omega \times (0, T), \tag{4.7}$$

where K_d^Θ $[m^3/kg]$ is the distribution coefficient for the temperature and D_m^Θ $[m^2/d]$ is the bulk thermal diffusivity. We propose to solve the system of partial differential equations (4.1), (4.2), (4.5) and (4.7) together with the boundary conditions

$$\begin{cases} h = h_D(\mathbf{x}, t) & \text{on } \partial\Omega_D^h \times (0, T), \\ \mathbf{q} \cdot \mathbf{n} = \bar{q}_N(\mathbf{x}, t) & \text{on } \partial\Omega_N^h \times (0, T), \\ C = C_D(\mathbf{x}, t) & \text{on } \partial\Omega_D^C \times (0, T), \\ \dfrac{\partial C}{\partial n} = \overline{C}_N(\mathbf{x}, t) & \text{on } \partial\Omega_N^C \times (0, T), \\ \Theta = \Theta_D(\mathbf{x}, t) & \text{on } \partial\Omega_D^\Theta \times (0, T), \\ \dfrac{\partial \Theta}{\partial n} = \overline{\Theta}_N(\mathbf{x}, t) & \text{on } \partial\Omega_N^\Theta \times (0, T), \end{cases} \tag{4.8}$$

where $\partial\Omega = \overline{\partial\Omega_D^h} \bigcup \overline{\partial\Omega_N^h} = \overline{\partial\Omega_D^C} \bigcup \overline{\partial\Omega_N^C} = \overline{\partial\Omega_D^\Theta} \bigcup \overline{\partial\Omega_N^\Theta}$ and where $\partial\Omega_D^h$, $\partial\Omega_D^C$ and $\partial\Omega_D^\Theta$ correspond to Dirichlet boundary conditions and $\partial\Omega_N^h$, $\partial\Omega_N^C$ and $\partial\Omega_N^\Theta$ correspond to Neumann boundary conditions for the hydraulic head h, the concentration C, and the temperature Θ respectively. The initial conditions are given by

$$\begin{cases} h(\mathbf{x},0) = h_{ini}(\mathbf{x}) & \text{in } \Omega, \\ C(\mathbf{x},0) = C_{ini}(\mathbf{x}) & \text{in } \Omega, \\ \Theta(\mathbf{x},0) = \Theta_{ini}(\mathbf{x}) & \text{in } \Omega. \end{cases} \tag{4.9}$$

4.2 Numerical approximation

4.2.1 Numerical approximation of the fluxes

We plug Darcy's law (4.2) into (4.1) and integrate over the volume element K for each $K \in \mathcal{M}$ to obtain

$$\begin{aligned} S_s \int_K \rho \frac{\partial h}{\partial t}\, d\mathbf{x} + \int_K \theta \frac{\partial \rho}{\partial C}\frac{\partial C}{\partial t}\, d\mathbf{x} - \sum_{\sigma\in\mathcal{E}_K} \int_\sigma \rho \frac{\mu_0}{\mu} \mathbf{K}_0 \nabla h \cdot \mathbf{n}_{K,\sigma}\, d\gamma \\ - \sum_{\sigma\in\mathcal{E}_K} \int_\sigma \rho \frac{\mu_0}{\mu} \mathbf{K}_0 \frac{\rho-\rho_0}{\rho_0} \nabla z \cdot \mathbf{n}_{K,\sigma}\, d\gamma = \int_K q_s \rho_s\, d\mathbf{x}. \end{aligned} \tag{4.10}$$

The diffusion flux $-\displaystyle\int_\sigma \rho \frac{\mu_0}{\mu} \mathbf{K}_0 \nabla h \cdot \mathbf{n}_{K,\sigma}\, d\gamma$ is approximated by the numerical flux $\rho_\sigma F_{K,\sigma}^h(h)$. More precisely

$$\rho_\sigma F_{K,\sigma}^h(h) = \rho_\sigma \frac{\mu_0}{\mu_\sigma} \sum_{\sigma'\in\mathcal{E}_K} A_K^{\sigma\sigma'}(h_K - h_{\sigma'}) \quad \text{for } h \in X_\mathcal{D}, \tag{4.11}$$

where the symmetric and positive-definite matrices $A_K^{\sigma\sigma'}$ are given by

$$A_K^{\sigma\sigma'} = \sum_{\sigma''\in\mathcal{E}_K} \mathbf{y}^{\sigma''\sigma} \cdot \Big(\int_{V_{K,\sigma''}} \mathbf{K}_0\, d\mathbf{x} \Big) \mathbf{y}^{\sigma''\sigma'}, \tag{4.12}$$

and $\mathbf{y}^{\sigma\sigma'}$ is given as in (2.4).

We integrate equations (4.5) and (4.7) over the volume element K for each $K \in \mathcal{M}$, to obtain

$$\begin{aligned} &\int_K (1 + \frac{\rho_b K_d^C}{\theta}) \frac{\partial(\theta C)}{\partial t}\, d\mathbf{x} + \sum_{\sigma\in\mathcal{E}_K} \int_\sigma \mathbf{q}\, C \cdot \mathbf{n}_{K,\sigma}\, d\gamma \\ &\qquad - \sum_{\sigma\in\mathcal{E}_K} \int_\sigma (\theta D_m^C + \mathbf{a}\cdot\mathbf{q}) \nabla C \cdot \mathbf{n}_{K,\sigma}\, d\gamma = \int_K q_s C_s\, d\mathbf{x}, \\ &\int_K (1 + \frac{\rho_b K_d^\Theta}{\theta}) \frac{\partial(\theta \Theta)}{\partial t}\, d\mathbf{x} + \sum_{\sigma\in\mathcal{E}_K} \int_\sigma \mathbf{q}\, \Theta \cdot \mathbf{n}_{K,\sigma}\, d\gamma \\ &\qquad - \sum_{\sigma\in\mathcal{E}_K} \int_\sigma (\theta D_m^\Theta + \mathbf{a}\cdot\mathbf{q}) \nabla \Theta \cdot \mathbf{n}_{K,\sigma}\, d\gamma = \int_K q_s \Theta_s\, d\mathbf{x}. \end{aligned} \tag{4.13}$$

In what follows we define the numerical fluxes $F^C_{K,\sigma}(C)$ and $F^\Theta_{K,\sigma}(\Theta)$ in order to approximate the diffusion fluxes $-\int_\sigma (\theta D^C_m + \mathbf{a}\cdot\mathbf{q})\nabla C\cdot\mathbf{n}_{K,\sigma}\,d\gamma$ and $-\int_\sigma (\theta D^\Theta_m + \mathbf{a}\cdot\mathbf{q})\nabla\Theta\cdot\mathbf{n}_{K,\sigma}\,d\gamma$ respectively. In view of the SUSHI scheme, we express the discrete fluxes $F^C_{K,\sigma}(C)$ and $F^\Theta_{K,\sigma}(\Theta)$ in terms of the discrete unknowns as:

$$F^C_{K,\sigma}(C) = \sum_{\sigma'\in\mathcal{E}_K} \overline{A}^{\sigma\sigma'}_K (C_K - C_{\sigma'}), \quad \overline{A}^{\sigma\sigma'}_K = \sum_{\sigma''\in\mathcal{E}_K} \mathbf{y}^{\sigma''\sigma}\cdot\Big(\int_{V_{K,\sigma''}} (\theta D^C_m + \mathbf{a}\cdot\mathbf{q})\,d\mathbf{x}\Big)\mathbf{y}^{\sigma''\sigma'}, \quad (4.14)$$

and

$$F^\Theta_{K,\sigma}(\Theta) = \sum_{\sigma'\in\mathcal{E}_K} \hat{A}^{\sigma\sigma'}_K (\Theta_K - \Theta_{\sigma'}), \quad \hat{A}^{\sigma\sigma'}_K = \sum_{\sigma''\in\mathcal{E}_K} \mathbf{y}^{\sigma''\sigma}\cdot\Big(\int_{V_{K,\sigma''}} (\theta D^\Theta_m + \mathbf{a}\cdot\mathbf{q})\,d\mathbf{x}\Big)\mathbf{y}^{\sigma''\sigma'}. \quad (4.15)$$

4.2.2 Numerical scheme

We remark that from [10], the derivatives $\frac{\partial\rho}{\partial h}$, $\frac{\partial\rho}{\partial C}$, $\frac{\partial\rho}{\partial\Theta}$ in the equation (4.3) and $\frac{\partial\mu}{\partial C}$ in the equation (4.4) are constants. We set $\theta_C = \theta + \rho_b K^C_d$ and $\theta_\Theta = \theta + \rho_b K^\Theta_d$ and present below a semi-implicit finite volume scheme corresponding to the system (4.1) - (4.7) with the boundary condition (4.8) and the initial conditions (4.9).

The initial conditions for the scheme are given by

$$h^0_K = \frac{1}{|K|}\int_K h_{ini}(\mathbf{x})\,d\mathbf{x}, \quad C^0_K = \frac{1}{|K|}\int_K C_{ini}(\mathbf{x})\,d\mathbf{x}, \quad \Theta^0_K = \frac{1}{|K|}\int_K \Theta_{ini}(\mathbf{x})\,d\mathbf{x}. \quad (4.16)$$

Next we present the discretized problem. For each $n\in\{1,...,N\}$:

Knowing h^{n-1},C^{n-1}, C^{n-2} and Θ^{n-1}, find $h^n\in X_D$ such that

$$\begin{cases} S_s|K|\rho^{n-1}_K(h^n_K - h^{n-1}_K) + \theta|K|\dfrac{\partial\rho}{\partial C}(C^{n-1}_K - C^{n-2}_K) + \delta t\displaystyle\sum_{\sigma\in\mathcal{E}_K} F^h_{K,\sigma}(h^n)\rho^{n-1}_\sigma \\ \qquad -\delta t\displaystyle\sum_{\sigma\in\mathcal{E}_K}\frac{\mu_0}{\mu^{n-1}_\sigma}\frac{\rho^{n-1}_\sigma-\rho_0}{\rho_0}\rho^{n-1}_\sigma(\mathbf{K}_0\nabla z)\cdot\mathbf{n}_{K,\sigma}|\sigma| = \rho_s Q^n_K \text{ for all } K\in\mathcal{M}, & (4.17a)\\ \displaystyle\sum_{K\in\mathcal{M}_\sigma}\Big\{F^h_{K,\sigma}(h^n)\rho^{n-1}_\sigma\Big\} = 0 \qquad \text{for all } \sigma\in\mathcal{E}_{int}, & (4.17b)\\ h^n_\sigma = h_D(\mathbf{x}_\sigma,t_n) \qquad \text{for all } \mathbf{x}_\sigma\in\partial\Omega^h_D, & (4.17c)\\ q^n_\sigma = |\sigma|\overline{q}_N(\mathbf{x}_\sigma,t_n) \qquad \text{for all } \mathbf{x}_\sigma\in\partial\Omega^h_N. & (4.17d)\end{cases}$$

where $Q^n_K = \displaystyle\int_{t^{n-1}}^{t^n}\int_K q_s\,d\mathbf{x}dt$, $F^h_{K,\sigma}(v)$, ρ^{n-1}_σ, and μ^{n-1}_σ are computed as (4.11), (4.19) and (4.20), respectively. We remark that when $n=1$, the term $(C^{n-1}_K - C^{n-2}_K)$ in equation (4.17a) is omitted. The approximate velocity q^n_σ is given by

$$q^n_\sigma = F^h_{K,\sigma}(h^n) - \frac{\mu_0}{\mu^{n-1}_\sigma}\frac{\rho^{n-1}_\sigma-\rho_0}{\rho_0}(\mathbf{K}_0\nabla z)\cdot\mathbf{n}_{K,\sigma}|\sigma|, \quad (4.18)$$

where

$$\rho_\sigma^n = \rho_0 + \frac{\partial \rho}{\partial C}(C_\sigma^n - C_0) + \frac{\partial \rho}{\partial \Theta}(\Theta_\sigma^n - \Theta_0) + \frac{\partial \rho}{\partial l}(h_\sigma^n - h_0), \tag{4.19}$$

and

$$\mu_\sigma^n = \frac{\partial \mu}{\partial C}(C_\sigma^n - C_0) + A_1 \cdot A_2^{\left(\frac{A_3}{\Theta_\sigma^n + A_4}\right)}. \tag{4.20}$$

Knowing q^n, C^{n-1}, find $C^n \in X_D$ such that

$$\begin{cases} \theta_C |K|(C_K^n - C_K^{n-1}) + \delta t \sum_{\sigma \in \mathcal{E}_K} q_\sigma^n \tilde{C}_{K,\sigma}^n \\ \qquad\qquad + \delta t \sum_{\sigma \in \mathcal{E}_K} F_{K,\sigma}^C(C^n) = C_s Q_K^n & \text{for all } K \in \mathcal{M}, \quad (4.21a) \\ \sum_{K \in \mathcal{M}_\sigma} \left\{ q_\sigma^n \tilde{C}_{K,\sigma}^n + F_{K,\sigma}^C(C^n) \right\} = 0 & \text{for all } \sigma \in \mathcal{E}_{int}, \quad (4.21b) \\ C_\sigma^n = C_D(\mathbf{x}_\sigma, t_n) & \text{for all } \mathbf{x}_\sigma \in \partial\Omega_D^c, \quad (4.21c) \\ F_{K,\sigma}^C(C^n) = -(\theta D_m^C + \mathbf{a} \cdot \frac{q_\sigma^n}{|\sigma|} \mathbf{n}_{K,\sigma}) |\sigma| \overline{C}_N(\mathbf{x}_\sigma, t_n) & \text{for all } \mathbf{x}_\sigma \in \partial\Omega_N^c. \quad (4.21d) \end{cases}$$

Knowing q^n, Θ^{n-1}, find $\Theta^n \in X_D$ such that

$$\begin{cases} \theta_\Theta |K|(\Theta_K^n - \Theta_K^{n-1}) + \delta t \sum_{\sigma \in \mathcal{E}_K} q_\sigma^n \tilde{\Theta}_{K,\sigma}^n \\ \qquad\qquad + \delta t \sum_{\sigma \in \mathcal{E}_K} F_{K,\sigma}^\Theta(\Theta^n) = \Theta_s Q_K^n & \text{for all } K \in \mathcal{T}, \quad (4.22a) \\ \sum_{K \in \mathcal{T}_\sigma} \left\{ q_\sigma^n \tilde{\Theta}_{K\sigma}^n + F_{K,\sigma}^\Theta(\Theta^n) \right\} = 0 & \text{for all } \sigma \in \mathcal{E}_{int}, \quad (4.22b) \\ \Theta_\sigma^n = \Theta_D(\mathbf{x}_\sigma, t_n) & \text{for all } \mathbf{x}_\sigma \in \partial\Omega_D^\Theta, \quad (4.22c) \\ F_{K,\sigma}^\Theta(\Theta^n) = -(\theta D_m^\Theta + \mathbf{a} \cdot \frac{q_\sigma^n}{|\sigma|} \mathbf{n}_{K,\sigma}) |\sigma| \overline{\Theta}_N(\mathbf{x}_\sigma, t_n) & \text{for all } \mathbf{x}_\sigma \in \partial\Omega_N^\Theta. \quad (4.22d) \end{cases}$$

The approximate fluxes $F_{K,\sigma}^C(v)$ and $F_{K,\sigma}^\Theta(v)$ are defined by (4.14) and (4.15), respectively. The three equations (4.17b), (4.21b) and (4.22b) come from the local conservation of the discrete fluxes on the interior edges. Note that we use an upwind scheme for the convection term in (4.21a) and (4.22a) with

$$\tilde{C}_{K,\sigma}^n = \begin{cases} C_K^n & \text{if } \quad q_\sigma^n > 0 \\ C_\sigma^n & \text{otherwise} \end{cases} \qquad \text{and} \qquad \tilde{\Theta}_{K,\sigma}^n = \begin{cases} \Theta_K^n & \text{if } \quad q_\sigma^n > 0 \\ \Theta_\sigma^n & \text{otherwise} \end{cases}$$

for each time step n.

5 Numerical tests

We propose an alternative simulation for the model problem developed in the SEAWAT documentation [10]. The problem consists in a two-dimensional cross section of a confined coastal aquifer initially saturated with relatively cold seawater at temperature $5°C$, so that $h_{ini} = 0$, $C_{ini} = 35$ and $\Theta_{ini} = 5$. Warmer fresh water at temperature $25°C$ is injected into the coastal aquifer along the left boundary to represent the flow from inland areas. The warmer fresh water flows to the right, where it discharges into a vertical ocean boundary. The ocean boundary is represented with hydrostatic conditions based on the fluid density calculated from the seawater salinity at $5°C$. No flow boundary conditions are assigned on the top and bottom boundaries. Because of the gravity and no flux boundary conditions at the top and bottom boundaries, the velocity is different at the top, bottom and middle of the aquifer. At the bottom, the flow is very slow so that the values of the concentration and of the temperature do not change much. At the top, the flux is very strong, so that the values of the concentration and of the temperature change fast. This problem is a simplified representation of what may occur in a coastal carbonate platform.

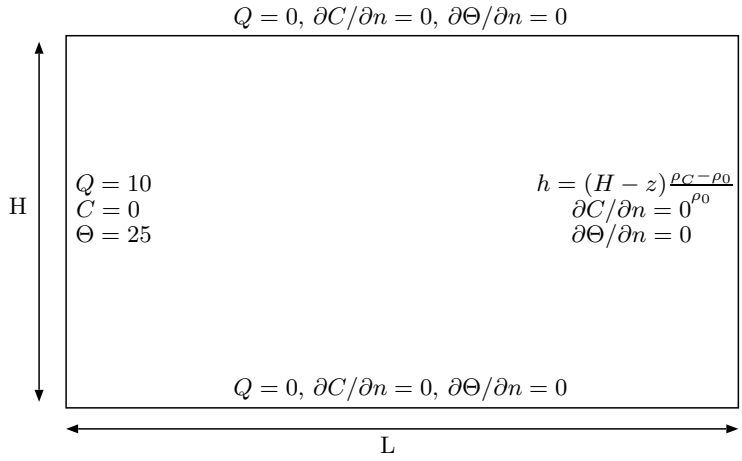

Figure 15: The boundary conditions of the model problem

The space domain is given by $L = 2000\ m$ and $H = 1000\ m$ and the boundary condition on the sea water boundary is given by $h(x = L, z) = (H - z) \cdot \frac{\rho_C - \rho_0}{\rho_0}$, where the elevation z is such that $0 \leq z \leq H$. The average flux velocity on the boundary $(x = 0, z)$ is given by $\overline{q}_N = \frac{Q}{H}$ with $Q = 10\, m^2/d$. And we have that $q_s = 0$.

The adaptive mesh is very efficient here, since the variations of the concentration and of the temperature only take place in their interface areas respectively. We present numerical simulations in three cases. For test cases 1 and 2 below, we neglect the heat transfer equation and consider the mesh refinement to be based on the variation of the concentration C. In test case 3, the interfaces of the concentration and of the temperature do not advance with the same speed, so that we perform a first computation with the refinement based on the variation of the concentration (Figures 21 and 22) and a second time computation with the

refinement based on the variation of the temperature in order to present the results on the temperature profiles (Figure 23).

We start from a uniform 40×20 square mesh to discretize the domain $(0, L) \times (0, H)$. We choose α close to 0.8 in order to make the refined-list long enough, and we choose β around 0.2 for the remerge list in order to keep the process stable.

5.1 Test case 1 and test case 2

In the first 2 test cases, we consider different expressions of the fluid density ρ and suppose that the fluid viscosity μ is constant, i.e. $\mu(\mathbf{x}, t) = \mu_0$ for all $\mathbf{x}$ and t. We neglect the heat transfer equation and consider the system

$$\begin{cases} S_s \rho \dfrac{\partial h}{\partial t} + \theta \dfrac{\partial \rho}{\partial C} \dfrac{\partial C}{\partial t} + \nabla \cdot (\mathbf{q}\rho) = q_s \rho_s \quad \text{in } \Omega \times (0, T), \\ (1 + \dfrac{\rho_b K_d^C}{\theta}) \dfrac{\partial (\theta C)}{\partial t} + \nabla \cdot (\mathbf{q}C) - \nabla \cdot \Big((\theta D_m^C + \mathbf{a} \cdot \mathbf{q}) \nabla C \Big) = q_s C_s \quad \text{in } \Omega \times (0, T). \end{cases} \tag{5.1}$$

We apply the scheme (4.17), (4.18) and (4.21) for the numerical simulations.

Test case 1: We suppose that the fluid density only depends on concentration C which can be rewritten as

$$\rho = \rho_0 + \frac{\partial \rho}{\partial C}(C - C_0). \tag{5.2}$$

The figures 16 and 17 show the time evolution of the concentration in test case 1.

Test case 2: In this test case, we consider the density ρ to be a linear function of concentration C and temperature Θ:

$$\rho = \rho_0 + \frac{\partial \rho}{\partial C}(C - C_0) + \frac{\partial \rho}{\partial \Theta}(\Theta - \Theta_0). \tag{5.3}$$

The value of the slope $\dfrac{\partial \rho}{\partial \Theta}$ is -0.375. The negative sign indicates that the fluid density increases as the temperature decreases, as shown in Figure 13(b). And the temperature is a simple linear function of the concentration:

$$\Theta = (\frac{\Theta_{inflow} - \Theta_{ocean}}{C_{inflow} - C_{ocean}})C + (\Theta_{inflow} - \Theta_{ocean}) = -\frac{4}{7}C + 20, \tag{5.4}$$

where $\Theta_{inflow} = 25^o C$, $\Theta_{ocean} = 5^o C$, $C_{inflow} = 0\, kg/m^3$ and $C_{ocean} = 35\, kg/m^3$. The figures 18 and 19 show the time evolution of the concentration in this test case.

Comparison between the test cases 1 and 2: we compare the numerical results obtained in the 2 cases: it turns out that the front displacement is lower in test case 2 than in test case 1; moreover we also observe that the transition front'sx width is thinner in test case 2. We then compare our results to those in SEAWAT [10]. The transient movement of the freshwater-saltwater transition zone in the simulations performed in SEAWAT corresponding test case 1 and test case 2 are shown as Figure 20. Our results look very similar to those of SEAWAT.

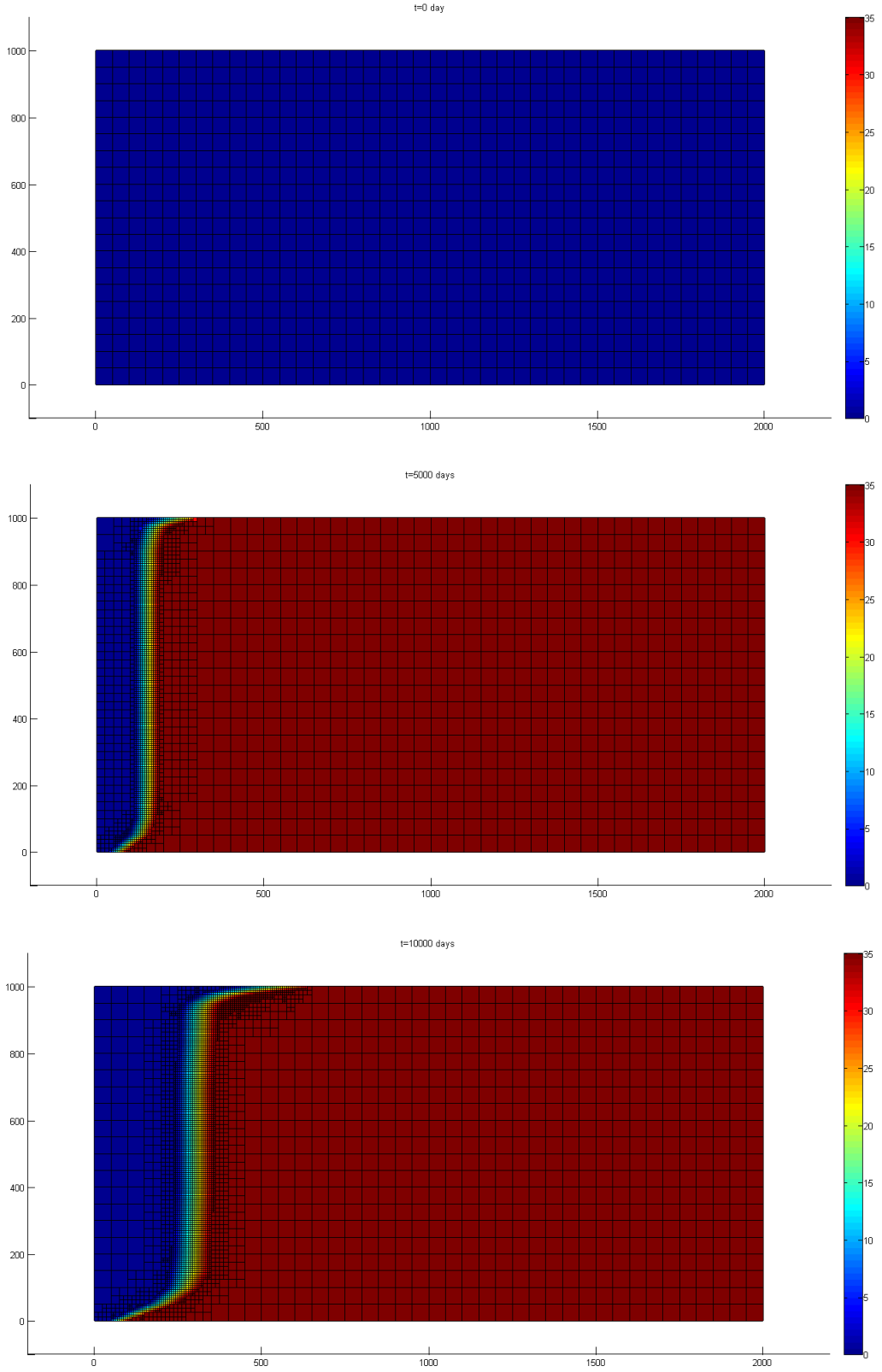

Figure 16: Concentration profiles at the initial time and at the times $t = 5000$ and $t = 10000$ days for test case 1.

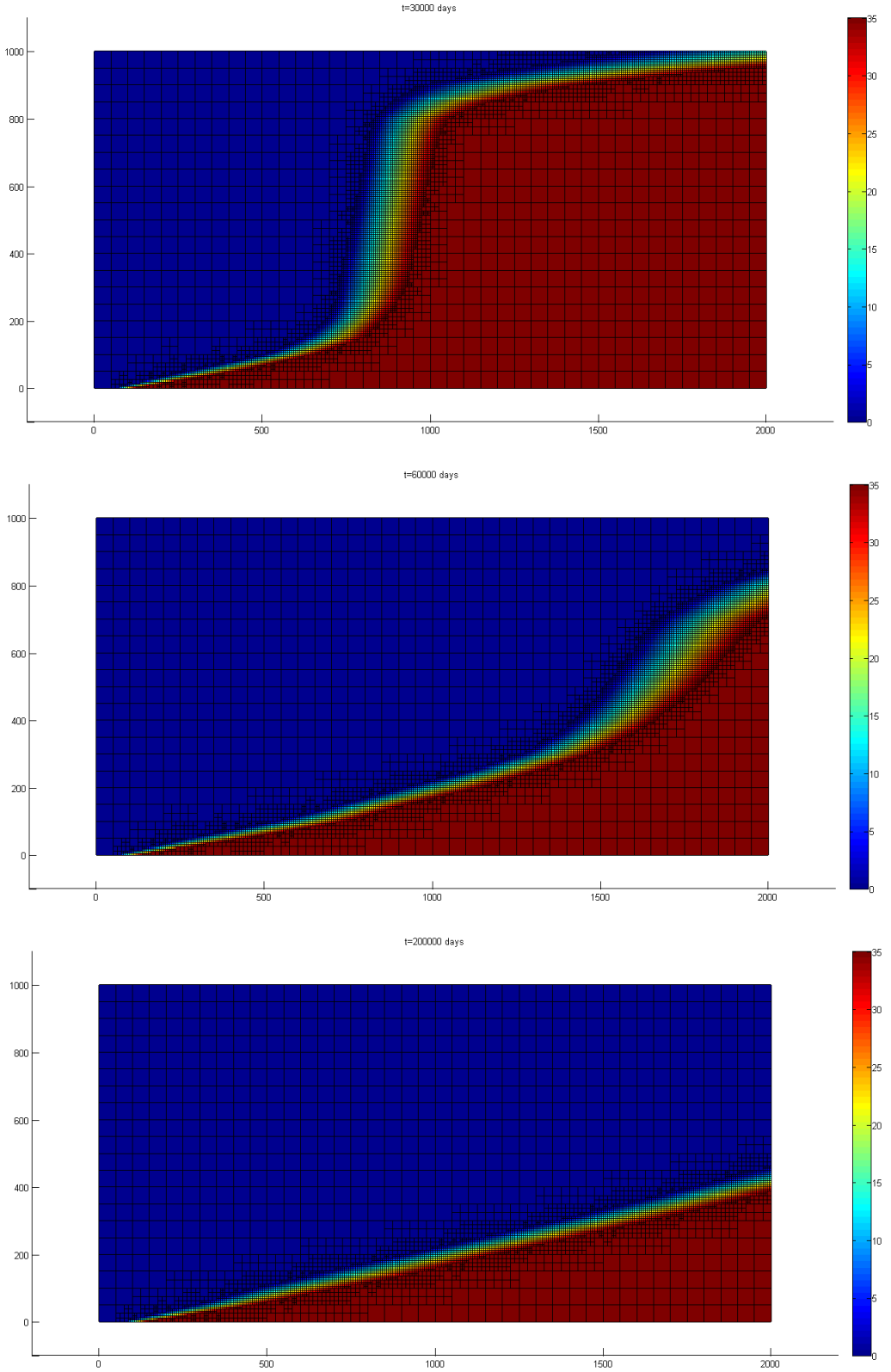

Figure 17: Concentration profiles at the times $t = 30000$, $t = 60000$ and $t = 200000$ days for test case 1.

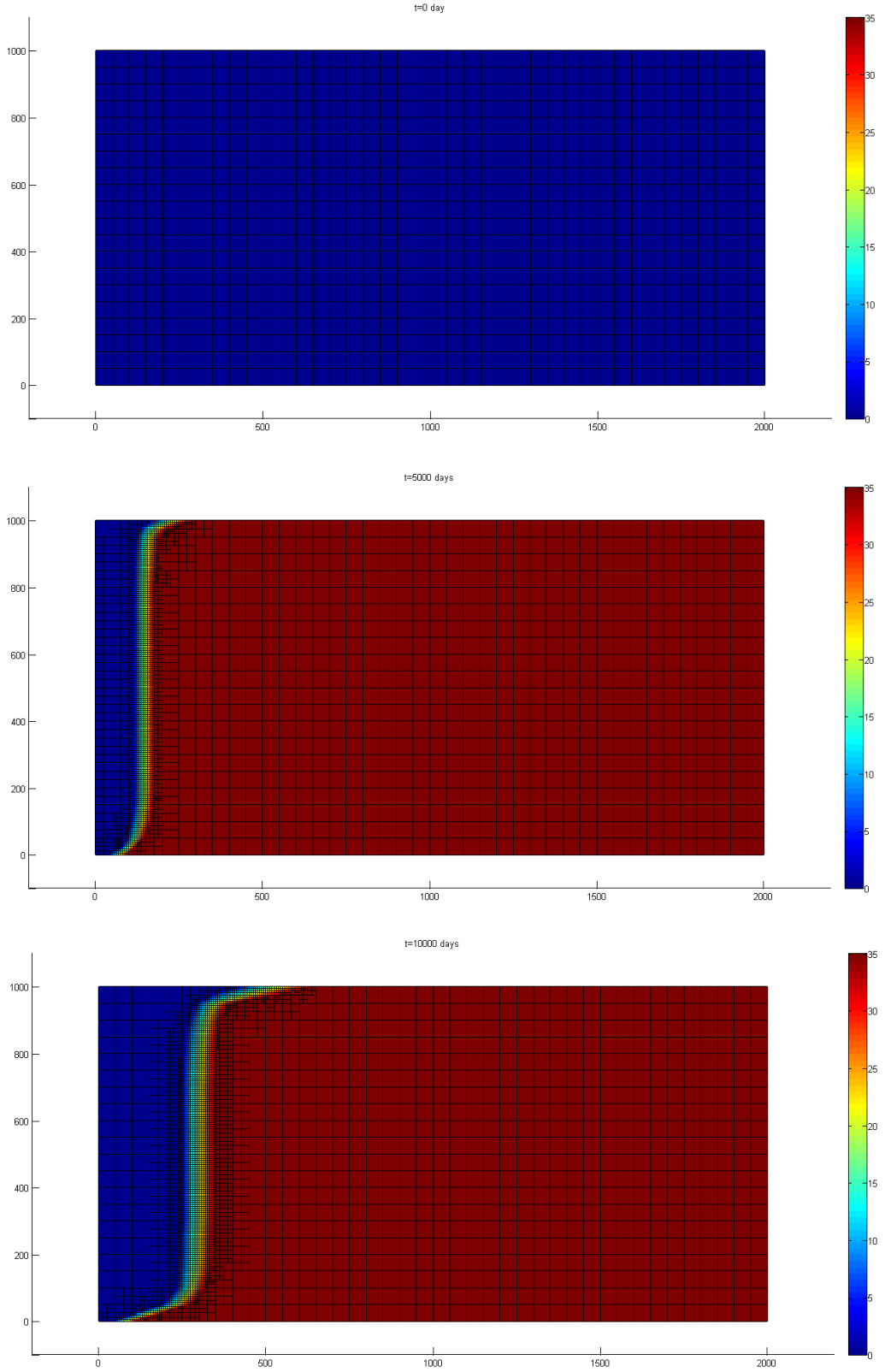

Figure 18: Concentration profiles at the initial time and at the times $t = 5000$ and $t = 10000$ days for test case 2.

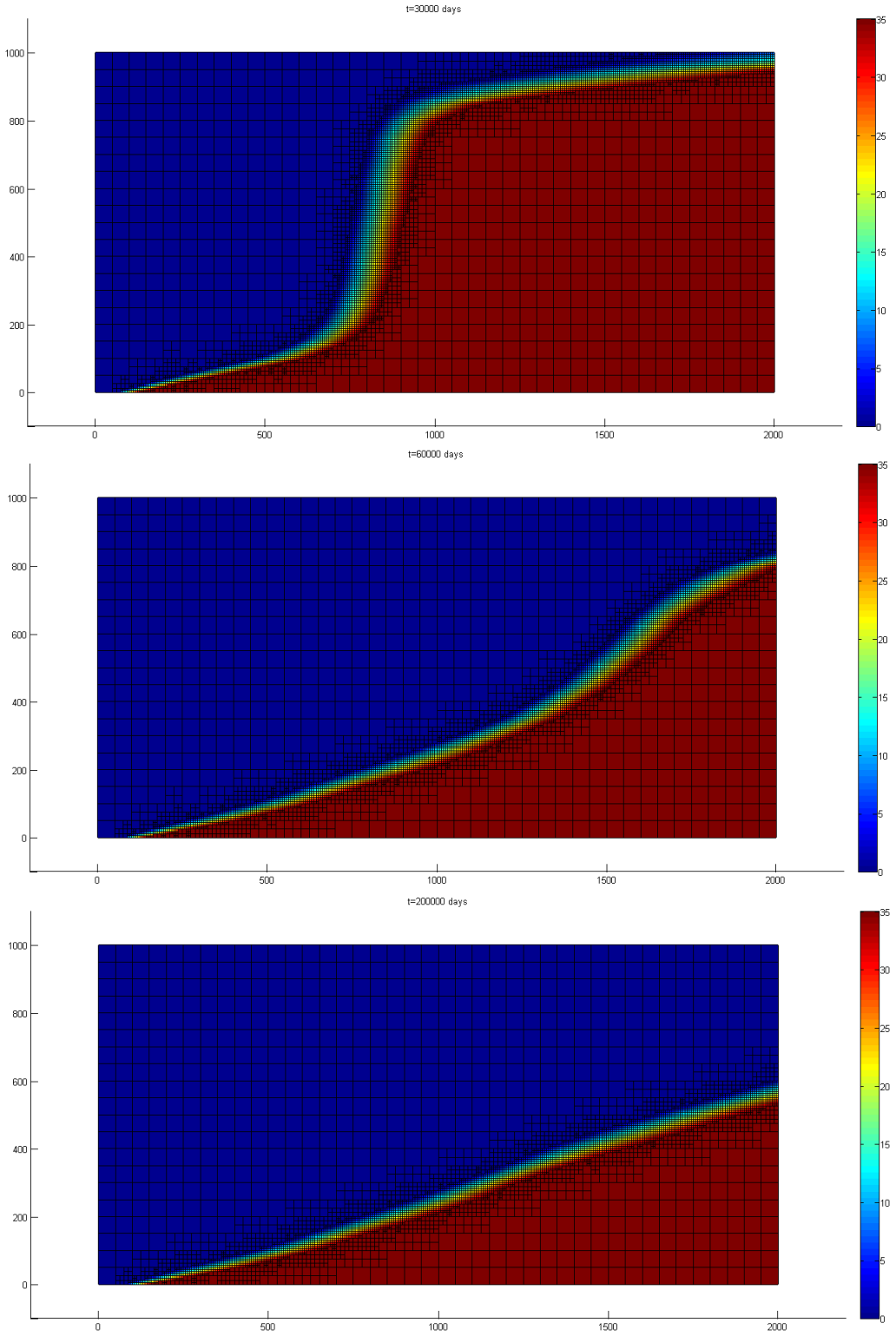

Figure 19: Concentration profiles at the times $t = 30000$, $t = 60000$ and $t = 200000$ days for test case 2.

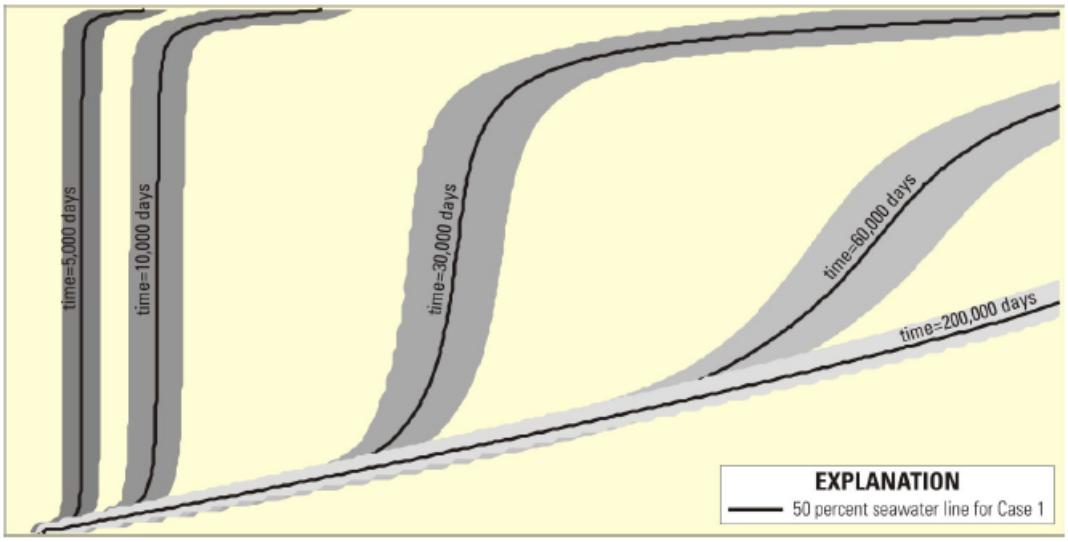

The transient motion of the freshwater-saltwater transition zone for test case 1 in SEAWAT.

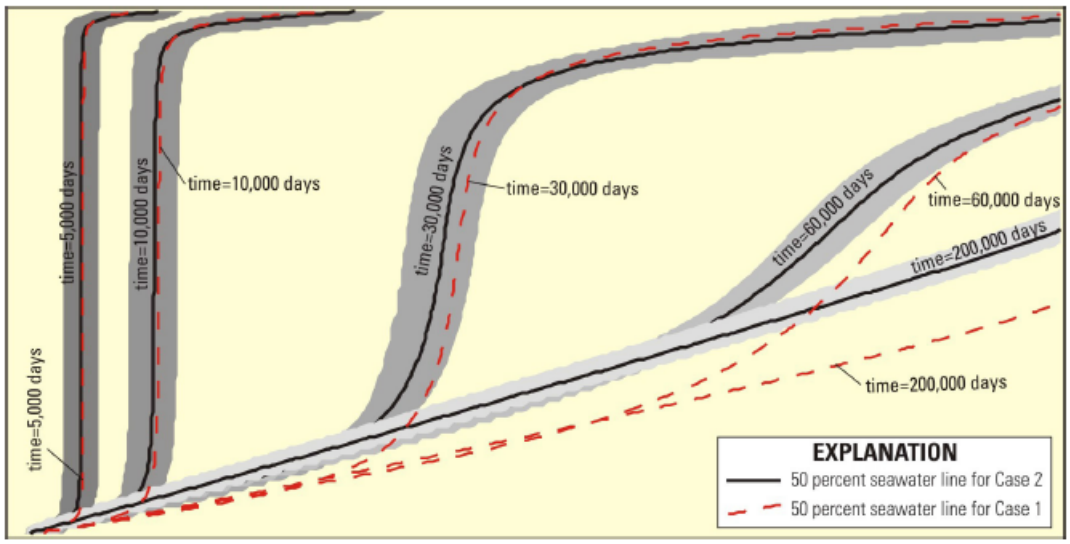

The transient motion of the freshwater-saltwater transition zone for test case 2 in SEAWAT.

Figure 20: Simulation for the test cases 1 and 2 using SEAWAT [10].

5.2 Test case 3

In this test case, we consider the system coupled with the heat transfer equation. Then the fluid density ρ is given by (4.3) and the viscosity μ is given by (4.4).

An adaptive mesh corresponding to the concentration variation is used for the simulations shown in the figures 21 and 22. Meanwhile we perform the simulation for a second time with an adaptive mesh corresponding to the temperature variation for the numerical results of temperature. The time evolution of the temperature is shown in Figure 23. Our result are compared to those in SEAWAT to show that both are similar. The transient motion of the freshwater-saltwater transition zone and that of temperature transition zone in SEAWAT corresponding to test case 3 are shown as Figure 24.

We remark that the width of the transition fronts of the concentration C is thicker in test case 3 where there is a coupling with the heat transport equation.

Parameter	**Value**	**Unit**
Specific storage S_s	1.00×10^{-5}.	$1/m$
Porosity θ	0.35	$-$
Reference viscosity μ_0	0.001	$kg/(m \cdot s)$
Reference density ρ_0	1000	kg/m^3
Bulk density ρ_b	1761.5	kg/m^3
Reference concentration C_0	0	kg/m^3
Reference temperature Θ_0	25	C
Horizontal hydraulic conductivity $\mathbf{K}_{h0}$	10	m/d
Vertical hydraulic conductivity $\mathbf{K}_{v0}$	0.1	m/d
Longitudinal dispersivity $\mathbf{a}_L$	1	m
Transverse dispersivity $\mathbf{a}_T$	0.1	m
Diffusion coefficient D_m^C	1.00×10^{-10}	m^2/d
Bulk thermal diffusivity D_m^Θ	0.150309621	m^2/d
Distribution coefficient for concentration K_d^C	0	m^3/kg
Distribution coefficient for temperature K_d^θ	2.00×10^{-4}	m^3/kg
A_1	2.394×10^{-5}	$-$
A_2	10	$-$
A_3	248.37	$-$
A_4	133.15	$-$
$\delta\mu/\delta C$	1.92×10^{-6}	m^2/d
$\delta\rho/\delta h$	4.46×10^{-3}	kg/m^4
$\delta\rho/\delta C$	0.7	$-$
$\delta\rho/\delta\Theta$	-0.375	$kg/(m^3 \cdot C)$

Table 7: Parameters of the model problem

The authors would like to thank Konstantin Brenner for indicating to them a number of references about density dependent flows in porous media, in particular [1] and the three

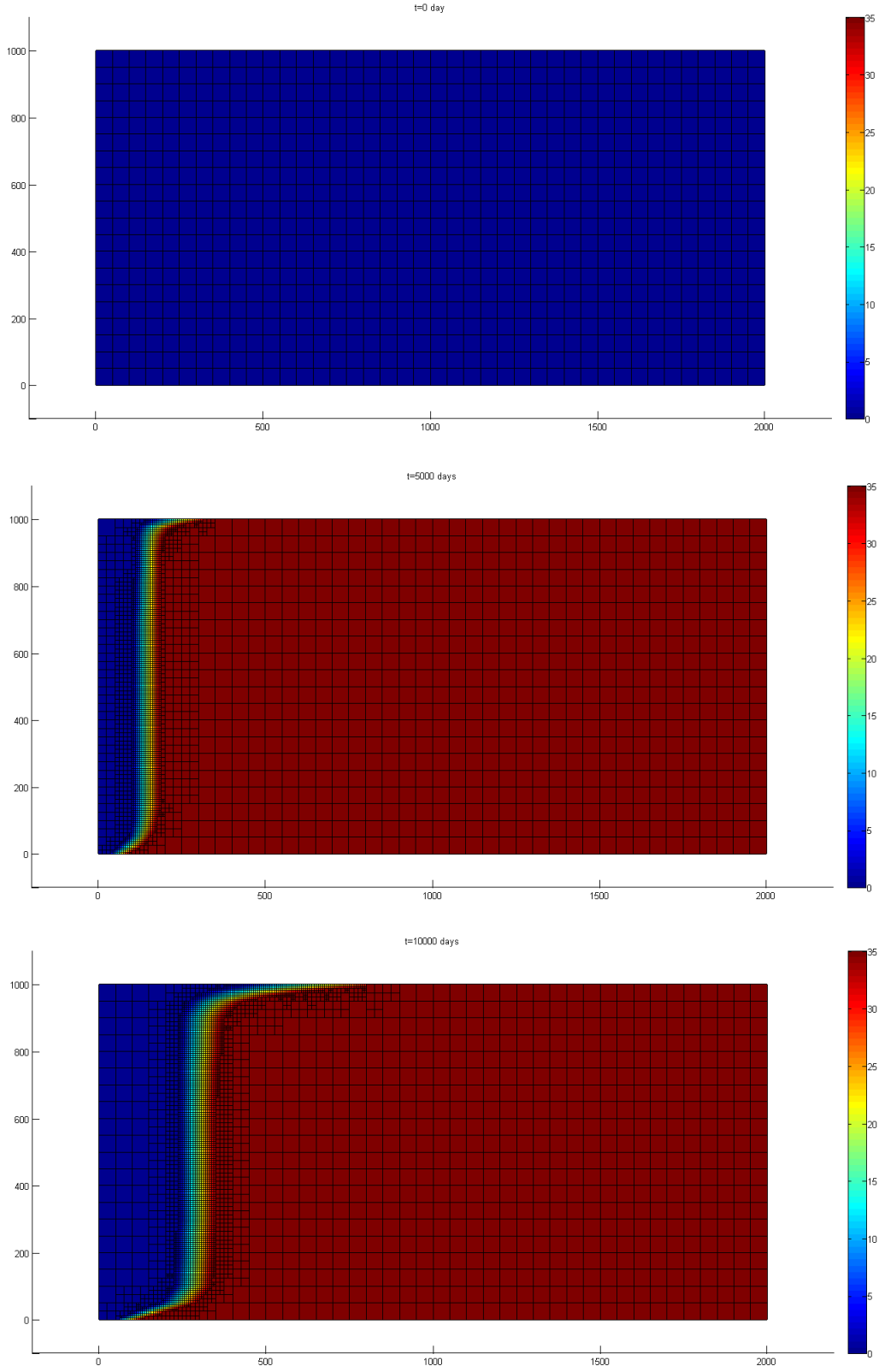

Figure 21: Concentration profiles at the initial time and at the times $t = 5000$ and $t = 10000$ days for test case 3.

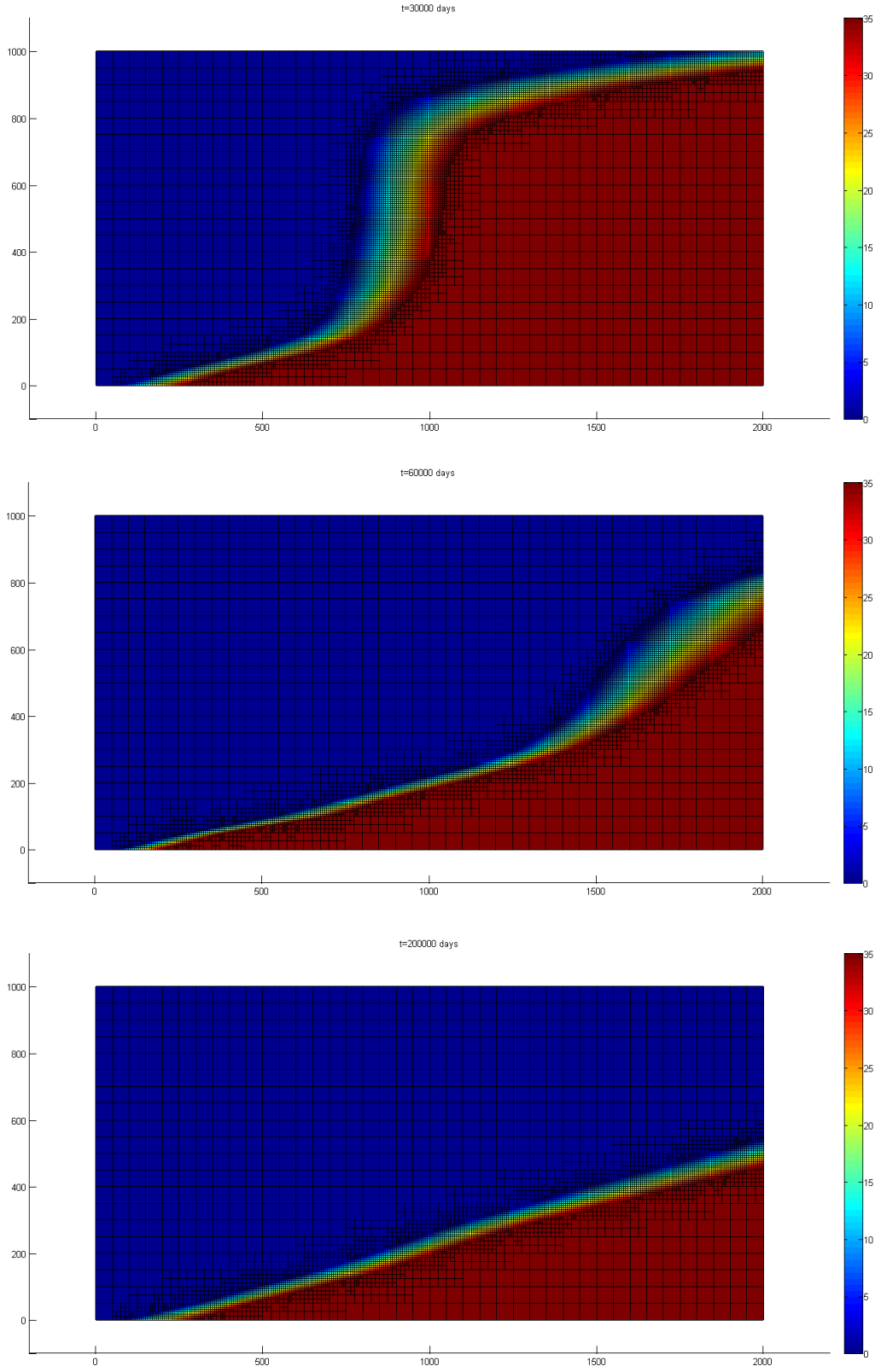

Figure 22: Concentration profiles at the times $t = 30000$, $t = 60000$ and $t = 200000$ days for test case 3.

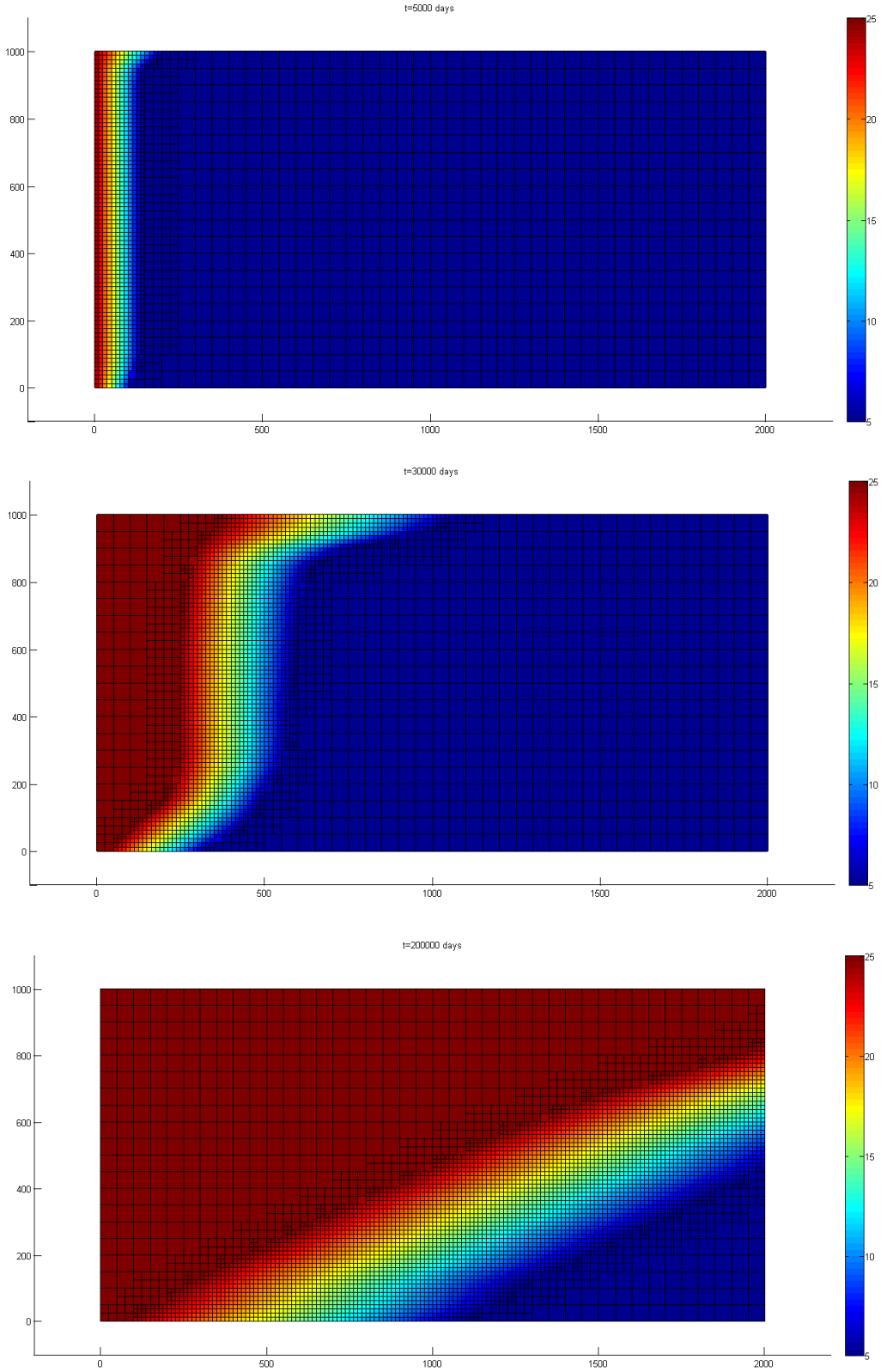

Figure 23: Temperature profiles at the time $t = 5000$, $t = 30000$ and $t = 200000$ days.

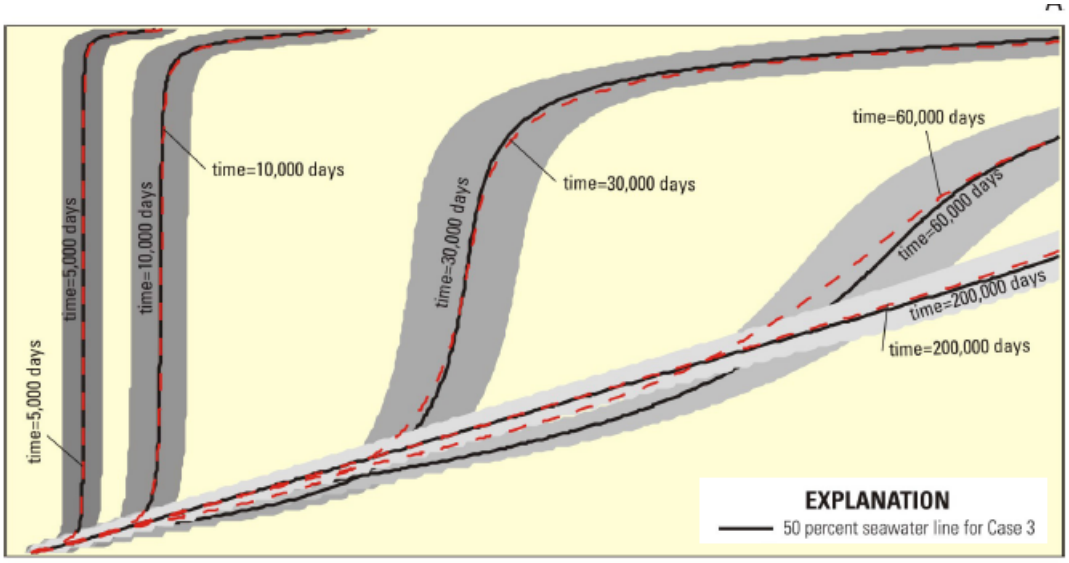

The transient motion of the freshwater-saltwater transition zone for test case 3 in SEAWAT.

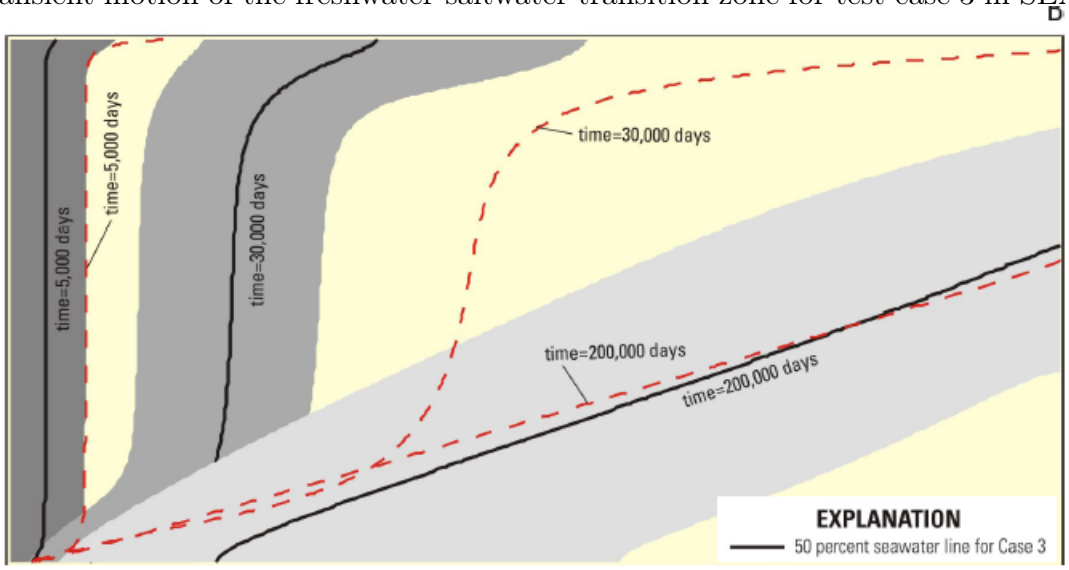

The transient motion of the temperature transition zone for test case 3 in SEAWAT.

Figure 24: Simulation for test case 3 using SEAWAT [10].

dimensional saltpool problem in this paper. They acknowledge the GDRI ReaDiNet for the financial support and for having provided opportunities of presenting the results.

References

[1] Bastian P.; Johannsen K.; Lang S.; Wieners C.; Reichenberger V.; Wittum G. High-accuracy simulation of density driven flow in porous media. In *High Performance Computing in Science and Engineering'01*; Jager, W.; Krause, E., Willi Eds.; Publisher: Springer-Verlag Berlin Heidelberg, 2002; pp. 500–511. DOI:10.1007/978-3-642-56034-7_50

[2] Bayer, U.; Clausnitzer V.; Fuhrmann J. Unsteady thermal convection in the North-East German basin. In *WIAS Preprint* **2002**; 741. DOI:10.23689/fidgeo-644

[3] Diersch, H.-J. G.; Kolditz, O. Variable-density flow and transport in porous media: Aproaches and Challenges. *Adv. Water Resour.* **2002**, *25*, 899–944. DOI:10.1016/S0309-1708(02)00063-5

[4] Eymard, R.; Gallouët, T.; Herbin, R. Discretization of heterogeneous and anisotropic diffusion problems on general nonconforming meshes SUSHI: a scheme using stabilization and hybrid interfaces. *IMA J. Numer. Anal.* **2010**, *30(4)*, 1009–1043. DOI:10.1093/imanum/drn084

[5] Feireisl, E.; Hilhorst, D.; Petzeltova, H.; Takac, P. Mathematical analysis of variable density flows in porous media. *J. Evol. Equ.* **2016**, *16*, 1–19. DOI:10.1007/s00028-015-0290-6

[6] Frind, E. O. Solution of long-term transient density-dependent transport in groundwater. *Adv. Water Resour.* **1982**, *5(2)*, 73–88. DOI:10.1016/0309-1708(82)90049-5

[7] Hilhorst, D.; Vu Do, H. C.; Wang, Y. A finite volume method for density driven flows in porous media. *ESAIM: Proc.* **2012** , *38*, 376–386. DOI:/10.1051/proc/201238021

[8] Hughes, J.D.; Sanford, W.E. SUTRA-MS a version of SUTRA modified to simulate heat and multiple solute transport. *US Geological Survey Open-File Report*, 2004-1207, U.S. Geological Survey, Reston, Virginia 2004.

[9] Johannesen, K.; Kinzelbach, W.; Oswald, S.; Wittum, G. The saltpool benchmark problem-Numerical simulation of saltwater upcoming in a porous medium. *Adv. Water Resour.* **2002**, *25(3)*, 335–348. DOI:10.1016/S0309-1708(01)00059-8

[10] C. D. Langevin, C. D.; Thorne Jr., D. T.; Dausman, A. M.; Sukop, M. C.; Guo, W. SEAWAT Version 4: A Computer Program for Simulation of Multi-Species Solute and Heat Transport. *Techiques and Methods Book 6; Chapter A22*. Publisher: Geological Survey (U.S.), 2008. DOI:10.3133/tm6A22

[11] Povich, T.J.; Dawson, C.N.; Farthing, M.W.; Kees, C.E. Finite element methods for variable density flow and solute transport. *Comput & Geosci.*, **2013**, *17*, 529–549. DOI:10.1007/s10596-012-9330-2

[12] Thorne, D.; Langevin, C.D.; M.C. Sukop, M.C. Addition of simultaneous heat and solute transport and variable fluid viscosity to SEAWAT. *Comput & Geosci.*, **2006**, *32*, 1758–1768. DOI: 10.1016/j.cageo.2006.04.005

[13] Voss, C.I. A finite-element simulation model for saturated-unsaturated, fluid-density-dependent ground-water flow with energy transport or chemically-reactive single-species solute transport. *U.S. Geological Survey Water-Resources Investigations Report*; Publisher: U.S. Geological Survey, 1984. DOI:10.3133/wri844369

[14] Vu Do, H.C. *Numerical methods for flow and transport in porous media*, Ph.D. Thesis; Université Paris-Sud, 2014